

# Generative Adversarial Networks (GAN) Powered Fast Magnetic Resonance Imaging — Mini Review, Comparison and Perspectives

Guang Yang<sup>1,2\*</sup>, Jun Lv<sup>3</sup>, Yutong Chen<sup>1,4</sup>, Jiahao Huang<sup>5</sup>, and Jin Zhu<sup>6</sup>

<sup>1</sup> National Heart & Lung Institute, Imperial College London, London SW7 2AZ, UK

<sup>2</sup> Cardiovascular Research Centre, Royal Brompton Hospital, London, SW3 6NP, UK

<sup>3</sup> School of Computer and Control Engineering, Yantai University, Yantai, China

<sup>4</sup> Department of Physiology, Development and Neuroscience, University of Cambridge, CB2 3EG, UK

<sup>5</sup> School of Optics and Photonics, Beijing Institute of Technology, Beijing, China

<sup>6</sup> Department of Computer Science and Technology, University of Cambridge, Cambridge, CB3 0FD, UK

**Abstract.** Magnetic Resonance Imaging (MRI) is a vital component of medical imaging. When compared to other image modalities, it has advantages such as the absence of radiation, superior soft tissue contrast, and complementary multiple sequence information. However, one drawback of MRI is its comparatively slow scanning and reconstruction compared to other image modalities, limiting its usage in some clinical applications when imaging time is critical. Traditional compressive sensing based MRI (CS-MRI) reconstruction can speed up MRI acquisition, but suffers from a long iterative process and noise-induced artefacts. Recently, Deep Neural Networks (DNNs) have been used in sparse MRI reconstruction models to recreate relatively high-quality images from heavily undersampled  $k$ -space data, allowing for much faster MRI scanning. However, there are still some hurdles to tackle. For example, directly training DNNs based on L1/L2 distance to the target fully sampled images could result in blurry reconstruction because L1/L2 loss can only enforce overall image or patch similarity and does not take into account local information such as anatomical sharpness. It is also hard to preserve fine image details while maintaining a natural appearance. More recently, Generative Adversarial Networks (GAN) based methods are proposed to solve fast MRI with enhanced image perceptual quality. The encoder obtains a latent space for the undersampling image, and the image is reconstructed by the decoder using the GAN loss. In this chapter, we review the GAN powered fast MRI methods with a comparative study on various anatomical datasets to demonstrate the generalisability and robustness of this kind of fast MRI while providing future perspectives.

**Keywords:** Generative Adversarial Networks (GAN); Fast Magnetic Resonance Imaging (MRI); Compressive Sensing; Deep Learning

---

\* Corresponding author: g.yang@imperial.ac.uk.

## 1 Introduction

### 1.1 Magnetic Resonance Imaging

Through offering repeatable, non-invasive measures of tissue structure and function, Magnetic resonance imaging (MRI) has transformed clinical medical imaging and medical science. The sensitivity of the image to tissue properties can be greatly varied with MRI, either by changing the timing with which MR signals are obtained (e.g., the echo time—TE and the repetition time—TR), or by using magnetisation preparation or contrast agents. These so-called multimodal or multi-sequence MRI methods can not only provide a comparison in traditional anatomical or structural MRI but can also quantify the function of most tissues and organs of the human body in clinical and pre-clinical laboratory environments. Invasive methods, such as tissue biopsy or radionuclide tests, have therefore become less needed as a result of the prosperity of MRI and other non-invasive medical imaging technologies [1]. Since MRI is non-invasive, it can be used to provide longitudinal and quantitative imaging biomarkers in the therapy trials. MR methods have begun to represent gold standard measurement for clinical research, despite the fact that the modality is still relatively underutilised [1]. Why is this so? 'MRI is complex and pricey,' which is a commonly heard melancholy.

### 1.2 Limitations of Magnetic Resonance Imaging

Although MRI is a revolutionary non-invasive diagnostic imaging technique that provides high-resolution definition of the structural and functional information of most body tissues and organs, one significant drawback of MRI is its slow rate of image acquisition, which results in a longer scanning period as compared to other imaging modalities [2,3].

In MRI, raw data is acquired in the  $k$ -space, which includes information about spatial frequencies within the image, rather than collected directly in the image space [4]. The Fourier transformation links image space and the  $k$ -space. The Nyquist criterion defines the  $k$ -space information that must be satisfied conventionally after we have defined the field-of-view (FOV) and spatial resolution of the image that we want to obtain. The distance between  $k$ -space neighbours is inversely proportional to the field of view in each direction. The highest frequency obtained in each direction is inversely proportional to the desired resolution. Data encoded with pulsed magnetic field gradients are acquired to fill the  $k$ -space. We may obtain a line of  $k$ -space points very quickly in one direction, known as the read direction, using either a spin or gradient echo in one repetition time. Further directions, on the other hand, must be phase-encoded, which takes one repetition time to encrypt one line of  $k$ -space lines [1,4]. This must then be rerun for all possible combinations of the number of phase encoding steps needed in the anterior-posterior and foot-head directions. As a result, MRI acquisitions can be time-consuming, particularly when a high resolution or large FOV is needed.

This drawback not only raises the cost of imaging but also limits its use in emergency situations. Furthermore, in order to maintain image consistency, patients must lie still during the acquisition. For abdominal/thoracic imaging, patients must hold their breath, which can be problematic for paediatric, obese patients, and those with respiratory compromise [1]. As a result, many patients can experience anxiety and claustrophobia during the MR scanning procedure [1]. In order to minimise scanning costs and increase patient throughput, the MR image acquisition process must be sped up. Various MR acceleration methods rely on taking measurements of several lines per repetition time, allowing for quicker traversing of the  $k$ -space. Examples include echo planar imaging [5], rapid acquisition with relaxation enhancement [6], and fast low angle shot imaging [7].

### 1.3 Conventional Acceleration Using Compressive Sensing

It is possible to attain a higher degree of acceleration by sampling the  $k$ -space only partially, i.e., not collecting all lines of measurements in the phase encoding path(s). The undersampled calculation can be used to infer the original  $k$ -space details. As a consequence, the acceleration metric is equal to the undersampling ratio. For example, if half of the  $k$ -space is sampled, the acceleration factor is doubled. As a result, undersampling methods aim to circumvent the Nyquist-Shannon sampling criterion [2].

Compressed sensing (CS) is a promising undersampling approach that may allow for more aggressive undersampling and acceleration [2]. CS principle is similar to the concept of compressing signals for transmission and then decompressing them [8], as seen in the JPEG, JPEG2000, MPEG, and MP3 standards [1]. If undersampled signals or images can be compressed correctly, they can also be decompressed or recovered accurately, according to CS [9]. Hereby, CS sets three conditions on the MRI reconstruction:

1. The image or signal must be compressible. In other words, the MRI images must be sparse, with the bulk of its pixel values being zeros, either in its native domain or in an appropriate transformation domain, such as in the wavelet or frequency domain.
2. To avoid aliasing artefacts, the undersampling patterns should be incoherent using random undersampling.
3. A non-linear reconstruction algorithm must be used.

It is possible to recover the original MRI images from their undersampled measurements following these three criteria.

Previously published research on using CS as an MR acceleration approach employs iterative non-linear optimisation algorithms that implement sparsity and reconstruction fidelity. Total variation (TV) [2], dictionary learning (DLMRI [10], RecPF [11], and BM3D [12]) are typical examples. However, there are four major issues with these approaches:

1. Iterative optimisation can be time-consuming [1,13].

2. These algorithms tend to generate artificially smoothed image appearance [1].
3. The reconstruction results can have blocky artefacts [14,15,16].
4. They reconstruct each image as an individual event, failing to account for the expected anatomical features in MR images that may be used to improve the reconstruction accuracy [17].

#### 1.4 Deep Learning Based Fast MRI

Deep learning based approaches have recently achieved performance dividends in a variety of medical image processing problems by using ‘big data’ and advancements in computational power. To date, however, the majority of research studies have concentrated on downstream medical image interpretation and post-processing activities, such as anatomical segmentation [18,19,20,21,22,23,24,25,26,27,28], lesion segmentation [29,30,31,32,33,34], co-registration [35,36,37], synthesis [38,39], and multimodal data detection [40,41,42,43,44,45,46], for disease identification [47,48,49], prognosis [50,51], and treatment prediction [52,53]. To increase the precision of these post-processing operations, imaging methods must be improved, which can also be aided by deep learning [54,55,56,57,58,59,60].

Since its principle was developed in 2006, CS has had a long history for fast imaging applications, including the embodiment of MRI reconstruction [61]. However, the related less efficient iterative optimisation can stymie further implementation. Although deep learning based tomographic reconstruction technology has only been around for a few years, there is a lot of interest in this area, and there are many ongoing advances and exciting applications, including MRI.

Deep learning based approaches can successfully overcome the majority of the aforementioned shortcomings of earlier CS methods. A deep learning algorithm, e.g., convolutional neural networks (CNN), is made up of many layers of nodes. To learn the mapping from undersampled MR images to their corresponding fully sampled ones, the weights of the node relations between layers are optimised. The method of optimising weights is known as training the model. Once trained, the model is capable of reconstructing original images from undersampled measurements. In terms of reconstruction accuracy, speed, and visual consistency, deep learning based methods have been shown to consistently outperform non-deep learning based ones [62,63,3,64,65,66].

#### 1.5 GAN Powered Fast MRI

Generative Adversarial Networks, or GAN for short, represent a type of generative modelling technique that employs deep learning methods, e.g., CNN. Generative modelling is an unsupervised learning task in machine learning that entails automatically finding and learning the regularities or patterns in input data such that the model can be used to produce or output new examples that could have been plausibly drawn from the original dataset.



GAN employs a clever method for training a generative model by posing the problem as a supervised learning problem with two sub-models: the generator model, which we train to produce new examples, and the discriminator model, which attempts to identify examples as either true (from the original domain) or false (generated). The two models are trained in an adversarial zero-sum game before the discriminator model is tricked about half of the time, indicating that the generator model is producing plausible instances.

GAN is a fascinating and quickly evolving area that delivers on the promise of generative models by producing plausible instances in a variety of problems, most notably in image-to-image conversion tasks such as translating image styles, and in generating photo-realistic images of objects, scenes, and individuals that even humans cannot recognise which ones are fake.

GAN is an important type of deep learning based CS-MRI reconstruction method, which was proposed first by Yang et al. in 2017 [67,3]. In the context of CS-MRI, GAN entails training a generator to recreate the original image from undersampled measurements and a discriminator to produce the likelihood of whether the generated image matches the original, i.e., fully sampled measurements. The discriminator, in turn, modifies the generator's learning [68]. As a consequence, the generator generates photo-realistic images [69]. In terms of reconstruction accuracy and efficiency, GAN based methods [3,62] outperform the non-GAN based deep learning method, e.g., deep ADMM-net. One GAN based approach [63] also claims to generate less fuzzy and aliasing artefacts than non-deep learning based methods. As a result, GAN based approaches have the capability to produce state-of-the-art CS-MRI reconstruction results.

In this book chapter,

- we will perform a mini topical review on GAN powered fast MRI, including the original Deep De-Aliasing Generative Adversarial Networks (DAGAN) method and other more advanced and recently proposed GAN based models;
- we will analyse and explain different GAN models, and compare the results obtained by different GAN based models;
- we will provide a comparison study on different datasets, e.g., MRI for various anatomical scans.
- we will highlight the recent development and discuss future directions.

## 2 Methods

### 2.1 Fundamentals of MRI Reconstruction

The basis of undersampled MR reconstruction is inferring the missing  $k$ -space data from the already sampled  $k$ -space values. For example, in partial Fourier imaging (PFI), 50% of the  $k$ -space is acquired. Because the  $k$ -space is conjugate symmetric, the other missing 50% is obtained via complex conjugation of the existing 50%. However, the maximum acceleration is only 2-fold and the reconstructed image exhibits a lower signal-to-noise ratio (SNR) [1]. Another key

undersampling technique is parallel imaging (PI). In PI, multiple receiver coils simultaneously collect the  $k$ -space information of the tissues closest to each coil. However, the acceleration factor is limited by the number and the configuration of the receiver coils [1,70]. Therefore, limits of accelerating MR image acquisition exist for both PI and PFI, bound by the Nyquist-Shannon sampling criteria [2].

Compressed sensing (CS)-based reconstruction circumvents the Nyquist-Shannon sampling criteria and achieves a higher acceleration ratio. CS establishes the model of MR image acquisition as (notations in Table 1):

$$y_u = Ax_t, \quad (1)$$

where  $y_u$  is the undersampled  $k$ -space signal and  $x_t$  is the original fully sampled image.  $A$  is an operator defined as:

$$A = \Psi\mathcal{F}, \quad (2)$$

where  $\Psi$  is the undersampling mask, a binary matrix denoting which  $k$ -space locations are sampled and which are not, and  $\mathcal{F}$  is the Fourier transform operator. Hence,  $\Psi\mathcal{F}x_t$ , or  $Ax_t$  is equivalent to undersampling the  $k$ -space of the putative reconstructed MR image.

A CS-model infers the underlying full resolution MR image  $x_t$  from the collected incomplete  $k$ -space samples  $y_u$  by solving the following optimisation problem [2]:

$$\arg \min_{\hat{x}_u} \frac{\lambda}{2} \|y_u - A\hat{x}_u\|_2^2 + R(\hat{x}_u), \quad (3)$$

where  $\lambda$  adjusts the contribution of the first term to the optimisation objective and  $R(\hat{x}_u)$  is an image regulariser function. If this reconstructed image  $\hat{x}_u$  is to match the original image, their undersampled  $k$ -space results ought to match, as reflected in the first term of Eq 3. This reinforces the  $k$ -space data fidelity of reconstructing the undersampled data.

The second term in Eq 3 ensures the reconstructed image possesses certain attributes such as smoothness or sparsity, which is required by the theory of CS. For example, total variation—an early CS technique—uses the following regulariser term to ensure the underlying image is smooth [2,71]:

$$\arg \min_{\hat{x}_u} \frac{\lambda}{2} \|y_u - A\hat{x}_u\|_2^2 + \|\nabla \hat{x}_u\|_1, \quad (4)$$

where  $\nabla$  is the gradient operator to minimise the difference between adjacent pixels in the final reconstruction to ensure a smooth texture. To solve Eq 4, conjugate gradient descent is employed [2], by updating the reconstructed image with the gradient of Eq 4 iteratively until convergence.

Another example of CS algorithm is dictionary learning, in which the regulariser function enforces the sparsity of the dictionary representation of each image patch [10]:

$$\arg \min_{\hat{x}_u, D, \Gamma} \frac{\lambda}{2} \|y_u - A\hat{x}_u\|_2^2 + \sum_{ij} \|R_{ij}\hat{x}_u - Da_{ij}\|_2^2, \quad (5)$$

where  $R_{ij}$  is the image patch extractor,  $D$  is the dictionary used to transform the dictionary representation  $a_{ij}$  into the image domain, and  $\Gamma$  is the set of all dictionary representations  $\{a_{ij}\}_{ij}$ . This optimisation problem in Eq 5 is solved by alternating minimisation of the 3 parameter sets iteratively:  $\hat{x}_u$ ,  $D$  and  $\Gamma$  collectively. CS algorithms such as TV and dictionary learning repeatedly update the reconstruction to ensure it fulfils  $k$ -space data fidelity and certain regularisation properties such as sparsity.

From a Bayesian perspective, data fidelity is seen as maximising the conditional probability of observing the undersampled  $k$ -space data given the reconstructed image. The regulariser term represents the prior expectation of the statistical properties of the final reconstructed image [72]. By jointly enforcing data fidelity and regulariser constraint, CS reconstruction is equivalent to maximising the posterior probability that the reconstructed image matches the original one given the existing  $k$ -space samples. This justifies the effectiveness of the CS in reconstructing undersampled MR images.

Symbol Definition	
$x_t$	Ground truth MR image
$x_u$	Undersampled MR image
$\hat{x}_u$	Reconstructed MR image
$y_t$	Ground truth $k$ -space signals
$y_u$	Undersampled $k$ -space signals
$\mathcal{F}$	Fourier transform operator
$\Psi$	Binary matrix denoting undersampled $k$ -space positions
$A$	$\Psi\mathcal{F}$
$R$	Regularisation function
$\lambda$	A parameter adjusting the contribution of data fidelity term to the reconstruction loss function
$\theta$	Parameters within a convolutional neural network

**Table 1.** Mathematical notations in this book chapter.

## 2.2 CNN Based MRI Reconstruction

CNN excels in computer vision applications compared to traditional machine learning methods in general, and has been increasingly incorporated into CS-based MRI reconstruction models. It achieves higher accuracy and acceleration of MRI acquisition compared to traditional CS models [3,66,64,73]. A CNN consists of a series of convolutional layers connected by non-linear activation functions [74]. In each convolutional layer, multiple filters are convolved with the input image or the output from a previous layer to extract image specific features [74]. The weight of each filter is optimised such that the final reconstructed image matches the original fully sampled image. By stacking multiple convolutional

layers, the large number of weight parameters in a CNN endows it with the potential to model complex functions, including recovering the fully sampled images from the undersampled ones.

The process of optimising the weights of CNN is known as training the network and is governed by an optimisation objective called the loss function. The loss functions differ between supervised and unsupervised settings, depending on whether fully sampled ground truth images are available. In a supervised learning setting, fully sampled images are used to “teach” the CNN model to minimise the loss, or difference, between the reconstructed results and the fully sampled ground truth. However, in an unsupervised environment, ground truth images are not available, meaning the loss function can be, for example, optimised based on the Deep Image Prior framework and uses a high-resolution reference MR image as the input of the CNN to induce the structural prior in the learning procedure [75]. Unsupervised CNN-based CS-MRI models are beyond the scope of this chapter, which will instead focus on the supervised learning models.

Supervised CNN-based CS-MRI methods can be broadly divided into two categories: end-to-end and unrolled optimisation [76,77,78]. End-to-end methods model the inverse of the acquisition process (Eq 1) by mapping the undersampled input to the reconstructed output directly, hence the name “end-to-end”:

$$\hat{x}_u = f_{\text{CNN}}(y_u|\theta), \quad (6)$$

where  $f_{\text{CNN}}$  is the operation performed by the CNN and  $\theta$  represents all the parameters within the CNN. The  $\theta$  is optimised by minimising the difference between  $\hat{x}_u$  and the ground truth  $x_t$ . Such end-to-end techniques are exemplified by U-Net [79] and generative adversarial network (GAN) [3,63,62].

In contrast, CNN-based unrolled optimisation methods perform iterative image update based upon the general CS reconstruction model (Eq 3). Unlike non-CNN based CS techniques, where the term  $R(\hat{x}_u)$  is an expert-designed regularisation function, the CNN-based unrolled methods apply CNN to learn the optimal way of regularising an image. This is exemplified by the deep cascade CNN (DC-CNN) network [64], whose regulariser term penalises the deviation of the reconstructed image from the CNN output:

$$\arg \min_{\hat{x}_u, \theta} \frac{\lambda}{2} \|y_u - A\hat{x}_u\|_2^2 + \|\hat{x}_u - f_{\text{CNN}}(y_u|\theta)\|. \quad (7)$$

Another example is the variational network [17], which uses a Field-of-Expert regularisation function:

$$\arg \min_{\hat{x}_u, \theta} \frac{\lambda}{2} \|y_u - A\hat{x}_u\|_2^2 + \sum_i f_i(k_i \hat{x}_u), \quad (8)$$

where  $f_i$  is a learnable activation function and  $k_i$  represents a convolutional filter. From a Bayesian point of view, these CNN-based regularisers form the prior expectation of the reconstructed images by learning from the ground truth MR images.

While both end-to-end and unrolled methods can incorporate CNN to learn the image reconstruction or regularisation process, a key difference between them is that unrolled methods need to iteratively update the images during the reconstruction process. In contrast, end-to-end ones compute the output directly. Hence, it is more time consuming to train unrolled CNN-based models and to apply them in reconstruction, compared with end-to-end methods, with other comparisons summarised in Table 2. This suggests an advantage of developing end-to-end methods, such as GAN-based models, for CS-MRI reconstruction.

Category	End-to-end Unrolled	
Reconstruction time	Short	Long
Data fidelity	No	Yes
Sample size	Larger	Smaller
Performance	Lower	Higher
Weight update	Yes	Yes
Image update	No	Yes
Parameter number	Larger	Smaller

**Table 2.** Comparison between end-to-end and unrolled optimisation methods in CNN-based CS-MRI models [76,77,78].

### 2.3 GAN Based MRI Reconstruction

**General GAN** Inspired by the two-player zero-sum game in game theory, GAN [68] consists of two players: a generator and a discriminator. Traditionally, the generator  $G$  captures the distribution of sample data, and uses noise  $z$  that follows a certain distribution to generate a sample  $G(z)$  similar to the real training data  $x_t$ . The discriminator  $D$  is a binary classifier, which aims to distinguish fake data generated by  $G$  from the ground truth. If the sample comes from the real training data,  $D$  outputs a large probability, otherwise,  $D$  outputs a small probability. Ideally, the best  $D$  can be represented as  $D(x_t) = 1$  and  $D(G(z)) = 0$ . In this way, the generator and the discriminator form a min-max game. The training process of GAN can be described as follows:

$$\min_{\theta_G} \max_{\theta_D} L(\theta_G, \theta_D) = \mathbb{E}_{\mathbf{x} \sim p_{\text{data}}(\mathbf{x})} [\log D_{\theta_D}(\mathbf{x})] + \mathbb{E}_{\mathbf{z} \sim p_{\mathbf{z}}(\mathbf{z})} [\log(1 - D_{\theta_D}(G_{\theta_G}(\mathbf{z})))] \quad (9)$$

where  $p_{\text{data}}(\mathbf{x})$  is the distribution of the training dataset, and the  $p_{\mathbf{z}}(\mathbf{z})$  is the distribution of the latent variables.

Alternating gradient optimisation between  $G$  and  $D$  is used to train the GAN. In this process, both models try their best to optimise their networks to form a competitive confrontation until the two models reach a dynamic balance.

Ideally, the final result is that the image generated by  $G$  is very similar to the real image, and it is difficult for the  $D$  network to distinguish between the real image and the image generated by  $G$ , i.e.,  $D(G(Z)) = 0.5$ .

**DAGAN** Deep De-Aliasing Generative Adversarial Networks (DAGAN) was proposed in 2017 by Yang et al. [3,67] for fast compressed sensing MRI reconstruction. Figure 1 shows the architecture of DAGAN.

As shown in Figure 2, a modified U-Net [80] was used as the generator  $G$ , which consisted of 8 convolutional layers in the encoding path and 8 deconvolutional layers in the decoding path. The stride of all convolutional and deconvolutional layers was set to 2 for downsampling and upsampling the feature maps. Each convolutional layer was followed by a Batch Normalisation (BN) layer and a Leaky ReLU (LReLU) layer. Skip connection was applied between corresponding layers in the encoding and decoding paths in order to pass the features in the encoding layer to the decoding layer for better reconstruction details. The modified U-Net ended up with a hyperbolic tangent function as the activation function. Due to the alternating training strategy in the adversarial components, the original GAN model is hard to train. DAGAN applied  $\hat{x}_u = G(x_u) + x_u$  instead of  $\hat{x}_u = G(x_u)$  as the output of the generator for better stability and faster convergence speed. In this way, DAGAN turned the generator into a refinement function, which means that it only generated the missing information, and the complexity of the model was reduced.

As shown in Figure 3, an 11-layer CNN architecture was used as the discriminator  $D$ . A BN layer and a LReLU layer were followed with each convolutional layer. Finally, a full connection (FC) layer was cascaded, and the classification result was output through the Sigmoid activation function.

In DAGAN, normalised MSE was used as the optimisation cost function. However, only optimising the pixel-wise MSE loss in the image domain could result in non-smooth reconstructions, which might lack coherent image details. To solve this problem, a data consistency loss was designed for training the generator in both frequency and image domains to help the optimisation and to exploit the complementary properties of the two domains. Besides, perceptual similarity [81] was also incorporated. In so doing, the data consistency loss consists of three parts: pixel-wise image domain MSE loss  $L_{\text{iMSE}}$ , frequency domain MSE loss  $L_{\text{fMSE}}$ , and the pre-trained VGG perceptual loss  $L_{\text{VGG}}$  [82]. They can be defined as:

$$L_{\text{iMSE}}(\theta_G) = \frac{1}{2} \|x_t - \hat{x}_u\|_2^2, \quad (10)$$

$$L_{\text{fMSE}}(\theta_G) = \frac{1}{2} \|\mathcal{F}x_t - \mathcal{F}\hat{x}_u\|_2^2, \quad (11)$$

$$L_{\text{VGG}}(\theta_G) = \frac{1}{2} \|f_{\text{VGG}}(x_t) - f_{\text{VGG}}(\hat{x}_u)\|_2^2. \quad (12)$$

Here,  $\|\cdot\|_2^2$  denotes the L2 norm,  $f_{\text{VGG}}(\cdot)$  denotes VGG network (the Conv4 output of the VGG16), and was pretrained on the ImageNet [83].

The adversarial loss  $L$  can be defined as:

$$L_{\text{adv}}(\theta_G, \theta_D) = \mathbb{E}_{x_t \sim P_{\text{train}}(x_t)} [\log D_{\theta_D}(x_t)] + \mathbb{E}_{x_u \sim p_G(x_u)} [\log(1 - D_{\theta_D}(G_{\theta_G}(x_u)))] \quad (13)$$

where  $P_{\text{train}}(x_t)$  denotes the collection of MR image ground truth, and  $p_G(x_u)$  denotes the collection of MR image reconstruction.

Therefore the total loss function can be represented as:

$$L_{\text{TOTAL}}(\theta_G, \theta_D) = \alpha L_{\text{iMSE}}(\theta_G) + \beta L_{\text{fMSE}}(\theta_G) + \gamma L_{\text{VGG}}(\theta_G) + L_{\text{adv}}(\theta_G, \theta_D), \quad (14)$$

where  $\alpha$ ,  $\beta$  and  $\gamma$  were the weights of different components of the loss function, which balanced different loss terms into similar scales according to previous study. Here,  $\alpha = 15$ ,  $\beta = 0.1$  and  $\gamma = 0.0025$  were set empirically, according to the original paper.

**KIGAN** KIGAN was introduced by Shaul et al. [84]. The overall structure of KIGAN is shown in Figure 4. A  $k$ -space generator  $G_K$  and an image space generator  $G_{\text{IM}}$  were cascaded in KIGAN. Adjacent undersampled  $k$ -space slices (along the third dimension or the temporal dimension)  $y_u^{l-1}$ ,  $y_u^l$  and  $y_u^{l+1}$  were the input of  $G_K$ . A data consistency step, i.e.,  $\tilde{y}_u = \bar{\Psi} G_K(y_u^{l-1}, y_u^l, y_u^{l+1}) + y_u^l$  was applied for merging the output with the reconstructed missing data.  $G_{\text{IM}}$  was able to generate the output of  $G_K$  in image space, i.e.,  $\tilde{x}_u$ , to reconstructed image  $\hat{x}_u$ . Refinement learning  $\hat{x}_u = G_{\text{IM}}(\tilde{x}_u) + \tilde{x}_u$  was also used as the output of  $G_{\text{IM}}$  instead of  $\hat{x}_u = G_{\text{IM}}(\tilde{x}_u)$ . The reconstruction MR image  $\hat{x}_u$ , together with MR ground truth image  $x_t$  were sent to the discriminator for the adversarial loss.

As shown in Figures 5 and 6, the main structure of the generators  $G_K$  and  $G_{\text{IM}}$  were based on a modified U-Net, which consisted of 5 convolutional layers in the encoding path and 5 deconvolutional layers in the decoding path, where each convolutional and deconvolutional layer were followed by a BN layer and a LReLU layer. Skip connection was applied between corresponding layers in the encoding and decoding paths, in order to pass the feature of different scales to the decoding layer for better reconstruction details. Additionally, in  $G_{\text{IM}}$ , a shortcut connection between the input and output was applied for turning  $G_{\text{IM}}$  into a refinement function.

As shown in Figure 7, the discriminator was a standard 9-layer CNN structure with an FC layer and a Sigmoid activation function connected for the result of the classification.

The loss function of KIGAN consisted of: an image domain MSE loss  $L_{\text{iMSE}}$ , a frequency domain MSE loss  $L_{\text{fMSE}}$ , and an adversarial loss  $L_{\text{adv}}$ , which can be defined as:

$$L_{\text{iMSE}}(\theta_K, \theta_{\text{IM}}) = \frac{1}{2} \|x_t - \hat{x}_u\|_2^2, \quad (15)$$

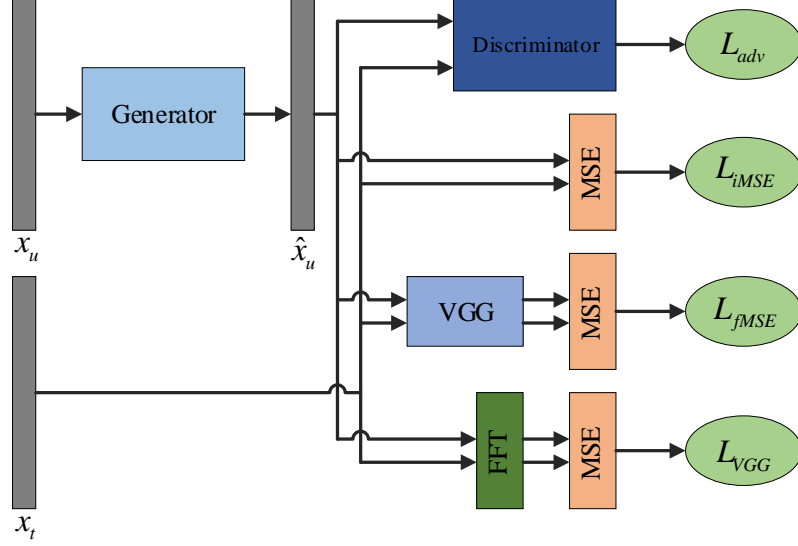


**Fig. 1.** The architecture of DAGAN. The generator produced the MR image  $\hat{x}_u$  from the undersampled MR image. The generated MR image  $\hat{x}_u$  and the ground truth MR image were input into the discriminator for adversarial loss  $L_{adv}$  calculation. The data consistency loss consisted of image domain MSE loss  $L_{iMSE}$ , frequency domain MSE loss  $L_{fMSE}$ , and VGG perceptual loss  $L_{VGG}$ .

$$L_{fMSE}(\theta_K) = \frac{1}{2} \|y_t^l - \tilde{y}_u\|_2^2, \quad (16)$$

$$L_{adv}(\theta_K, \theta_{IM}, \theta_D) = \mathbb{E}_{x_t \sim M}[\log D_{\theta_D}(x_t)] + \mathbb{E}_{\hat{x}_u \sim S}[\log(1 - D_{\theta_D}(\hat{x}_u))], \quad (17)$$

where  $M$  denotes the collection of image space ground truth, and  $S$  denotes the collection of image space reconstruction.

The whole loss function can be represented as:

$$L_{TOTAL}(\theta_K, \theta_{IM}, \theta_D) = \alpha L_{iMSE}(\theta_K, \theta_{IM}) + \beta L_{fMSE}(\theta_K) + L_{adv}(\theta_K, \theta_{IM}, \theta_D), \quad (18)$$

where  $\alpha, \beta$  are the hyperparameters that control the balance of different components in the loss function.



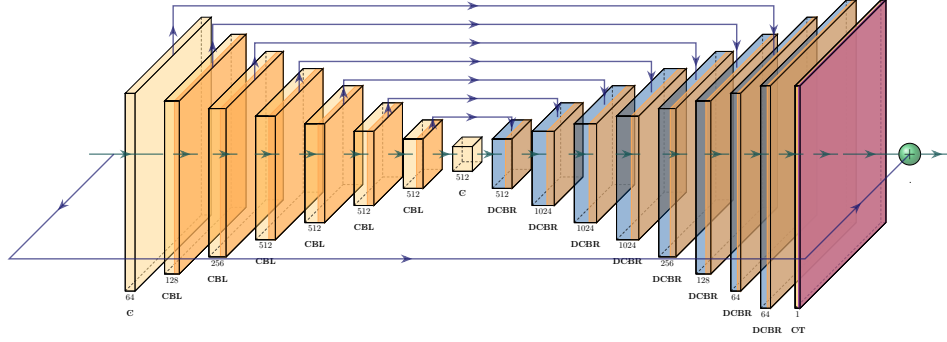


**Fig. 2.** Structure of the generator in DAGAN. The generator was based on a modified U-Net, which consisted of 8 convolutional layers and 8 transposed convolutional layers (de-convolutional layers), with a BN layer and a LReLU or ReLU layer followed with each layer. Skip connection between layers that were the same scale and shortcut connections between the input and output of the generator were applied. A hyperbolic tangent function was used as an output activation function. (C: Convolutional layer; DC: De-Convolutional layer; B: Batch Normalization layer; L: Leaky ReLU layer; R: ReLU layer; T: hyperbolic tangent function.)

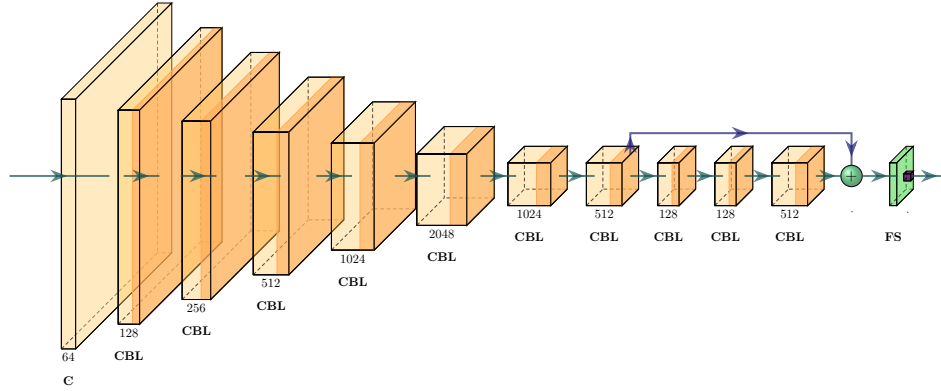


**Fig. 3.** Structure of the discriminator in DAGAN. Essentially, the discriminator was an 11-layer CNN classifier. Each convolutional layer was cascaded by a BN layer and a LReLU Layer. A full connection layer and a Sigmoid function were applied to output the result of the classification. (C: Convolutional layer; B: Batch Normalization layer; L: Leaky ReLU layer; F: Full Connection layer; S: Sigmoid function.)

**ReconGAN/RefineGAN** ReconGAN/RefineGAN was proposed by Quan et al. [62] for compressed sensing MRI reconstruction. Figure 8 shows the architecture of ReconGAN/RefineGAN. The two-fold chained network that consisted of 2 U-shaped generators ( $G_1$  and  $G_2$  respectively) was able to generate a 2-channel

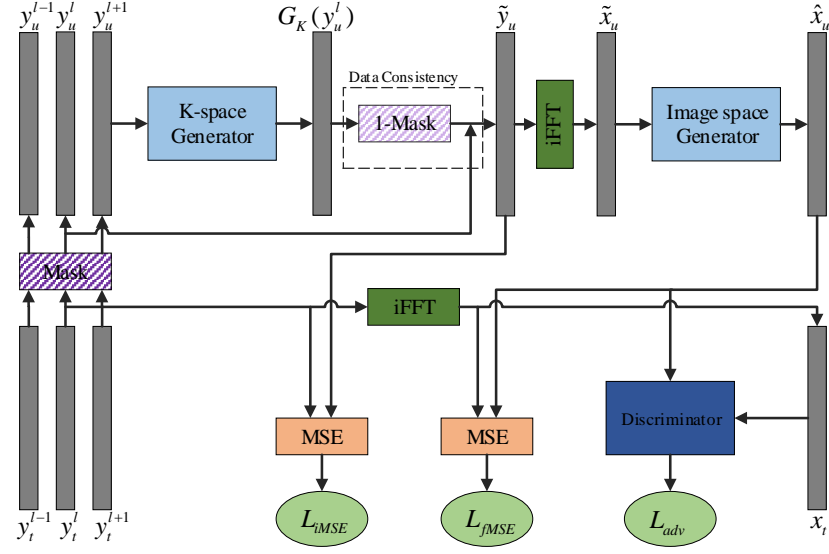


**Fig. 4.** The Architecture of KIGAN. Two generators and one discriminator were used in KIGAN.  $k$ -space generator was able to reconstruct  $k$ -space MR data  $G_K(y_u^l)$  from a cascade of undersampled  $k$ -space MR data  $y_u^{l-1}$ ,  $y_u^l$  and  $y_u^{l+1}$ , and image space generator was able to reconstruct the MR image  $\hat{x}_u$  (final result). The discriminator was to output the classification result of ground truth MR image  $x_t$  and generated MR image  $\hat{x}_u$  for adversarial loss  $L_{loss}$ . Image domain MSE loss  $L_{iMSE}$  and frequency domain MSE loss were added into the total loss function.

zero-filling MR image (real part and imaginary part) directly into a 2-channel reconstructed MR image. The checkpoints after  $G_1$  and  $G_2$  were defined as ReconGAN and RefineGAN respectively.

As shown in Figure 9, the generator consisted of 4 encoder blocks in the encoding path and 4 decoder blocks in the decoding path. Skip connection between corresponding blocks that had the same scale was adopted to pass the feature from the encoding path to the decoding path.  $\tilde{x}_u = G_1(x_u) + x_u$  and  $\hat{x}_u = G_2(\tilde{x}_u) + \tilde{x}_u$  were used as the output of the generator instead of  $\tilde{x}_u = G_1(x_u)$  and  $\hat{x}_u = G_2(\tilde{x}_u)$  for better reconstruction details and faster convergence speed. Figures 10 and 11 show the structure of the encoder block and decoder block. The encoder block consisted of 2 convolutional layers and a residual block inserted between them. The stride of the first convolutional layer was set to 2 for the downsampling. The decoder block consisted of 2 transposed convolutional layers and a residual block inserted between them. The stride of the second transposed convolutional layer was set to 2 for upsampling. The residual block consisted of three convolutional layers, the kernel number in the second convolutional layer was half of the kernel number in the first and third convolu-

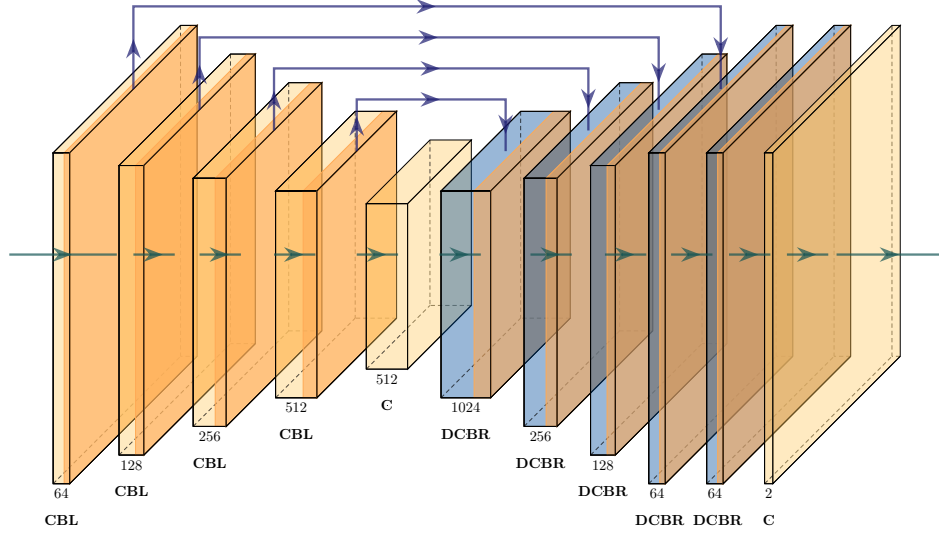


**Fig. 5.** The Structure of  $k$ -space Generator in KIGAN. Five convolutional layers and five de-convolutional layers were applied as encoding path and decoding path in the generator respectively. A convolutional layer was used as the output layer to adjust the channel of the reconstructed MR image. Corresponding layers of the same scales were linked by the skip connection. (C: Convolutional layer; DC: De-Convolutional layer; B: Batch Normalization layer; L: Leaky ReLU layer; R: ReLU layer.)

tional layer. A shortcut connection was linked between the input and output of the residual block.

As shown in Figure 12, the encoding path in the generator was adopted as the main structure of the discriminator. An FC layer and Sigmoid function were cascaded after the encoding path for the classification result.

The loss function of ReconGAN/RefineGAN was consisted of: image domain MSE loss  $L_{\text{iMSE}}$ , frequency domain MSE loss  $L_{\text{fMSE}}$ , and the adversarial loss  $L_{\text{adv}}$ , which can be defined as:

$$L_{\text{iMSE}}(\theta_{G_1}, \theta_{G_2}) = \frac{1}{2} \|x_t - \hat{x}_u\|_2^2, \quad (19)$$

$$L_{\text{fMSE}}(\theta_{G_1}, \theta_{G_2}) = \frac{1}{2} \|\mathcal{F}x_t - \mathcal{F}\hat{x}_u\|_2^2, \quad (20)$$

$$L_{\text{adv}}(\theta_{G_1}, \theta_{G_2}, \theta_D) = \mathbb{E}_{x_t \sim P_{\text{train}}(x_t)} [\log D_{\theta_D}(x_t)] + \mathbb{E}_{x_u \sim p_{G_2 G_1}(x_u)} [\log(1 - D_{\theta_D}(G_{\theta_{G_2}}(G_{\theta_{G_1}}(x_u)))]. \quad (21)$$

The total loss function can be represented as:

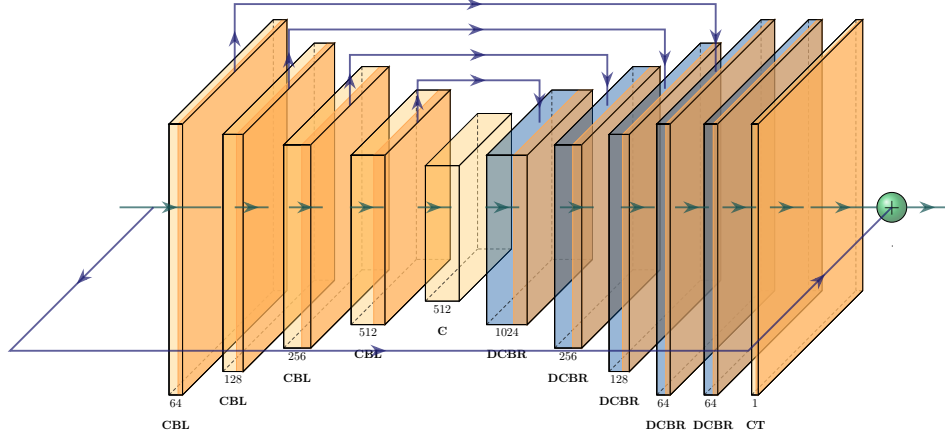


**Fig. 6.** The Structure of image space Generator in KIGAN. 5 convolutional layers and 5 de-convolutional layers were applied as encoding path and decoding path in the generator respectively. A convolutional layer and a hyperbolic tangent function were used as the output layer. Skip connection and shortcut connection were adopted in the image space generator. (C: Convolutional layer; DC: De-Convolutional layer; B: Batch Normalization layer; L: Leaky ReLU layer; R: ReLU layer; T: hyperbolic tangent function.)

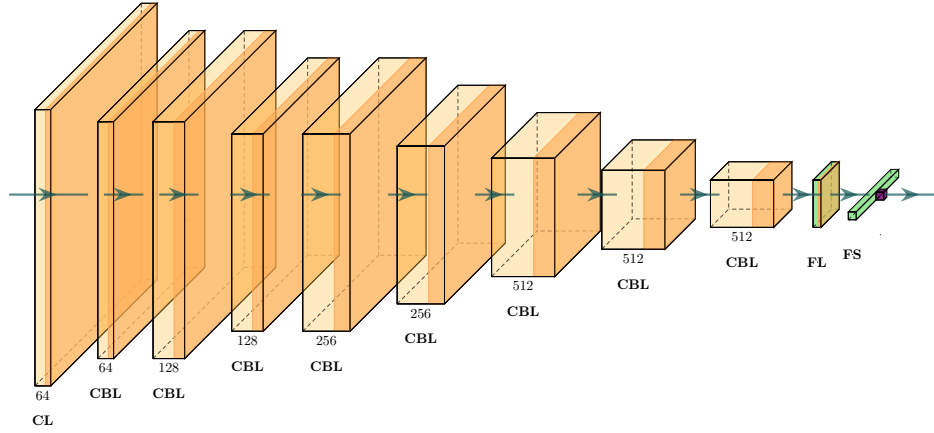


**Fig. 7.** The Structure of Discriminator in KIGAN. The discriminator was a standard 9-layer CNN structure with an FC layer and a Sigmoid activation function connected for the result of the classification. (C: Convolutional layer; B: Batch Normalization layer; L: Leaky ReLU layer; F: Full Connection layer; S: Sigmoid function.)

$$L_{\text{TOTAL}}(\theta_{G_1}, \theta_{G_2}, \theta_D) = \alpha L_{\text{iMSE}}(\theta_{G_1}, \theta_{G_2}) + \beta L_{\text{fMSE}}(\theta_{G_1}, \theta_{G_2}) + L_{\text{adv}}(\theta_{G_1}, \theta_{G_2}, \theta_D), \quad (22)$$

where  $\alpha = 10$ ,  $\beta = 0.1$  were the hyperparameters that controlled the balance of different components in the loss function.

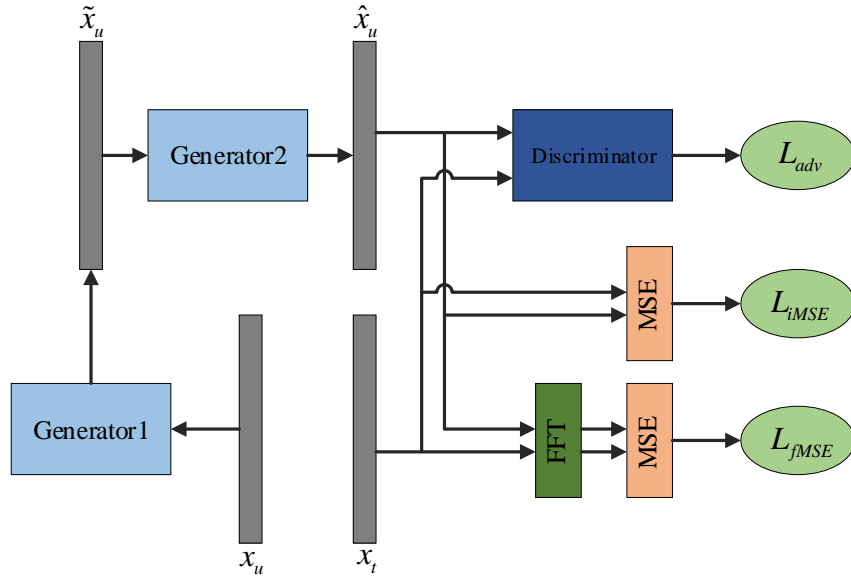


**Fig. 8.** The architecture of ReconGAN/RefineGAN. A two-fold chained network with 2 generators cascaded was used as the generator to produce reconstructed MR images  $\hat{x}_u$  from undersampled MR images  $x_u$ . Reconstructed MR images  $\hat{x}_u$  together with ground truth MR images  $x_t$  were sent to the discriminator for the calculation of the adversarial loss  $L_{\text{adv}}$ . Besides, image domain MSE loss  $L_{\text{iMSE}}$  and frequency domain MSE loss  $L_{\text{fMSE}}$  were added to the total loss function for training the generator.

## 2.4 Evaluation Methods

Generally, the evaluation methods include objective methods for fidelity quality assessment and subjective methods for perceptual quality assessment. In this section, we review the most popular metrics for fast MRI quality evaluation.

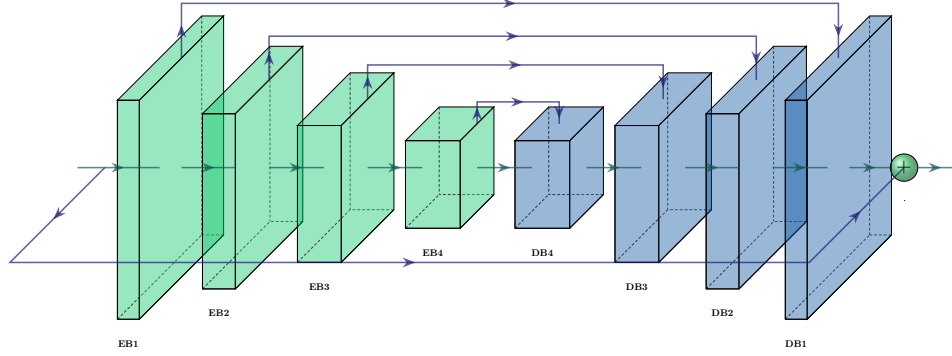


**Fig. 9.** Structure of the generator in ReconGAN/RefineGAN. The generator consisted of 4 encoder blocks in the encoding path and 4 decoder blocks in the decoding path. Skip connection was linked between blocks of the same scale in different paths. A shortcut connection was applied between the input and output of the generator, which turns the generator into a refinement function. (EB: Encoder Block; DB: Decoder Block.)

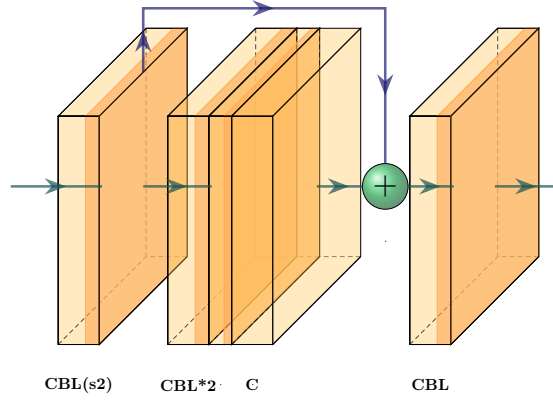


**Fig. 10.** Structure of the encoder block in the generator of ReconGAN/RefineGAN. (C: Convolutional layer; B: Batch Normalization layer; L: Leaky ReLU layer.)

**Fidelity Quality Assessment** First, we introduce the Peak Signal-to-Noise Ratio (PSNR), which is the most commonly used evaluation criteria for image transformation tasks (e.g., reconstruction, super-resolution, de-noising). It involves the data range to measure the pixel-level Mean Squared Error (MSE):

$$\text{PSNR}(I_{\text{rec}}, I_{\text{gt}}) = 10 \cdot \log_{10} \left( \frac{L^2}{\frac{1}{N} \sum_{i=1}^N (I_{\text{rec}}(i) - I_{\text{gt}}(i))^2} \right), \quad (23)$$

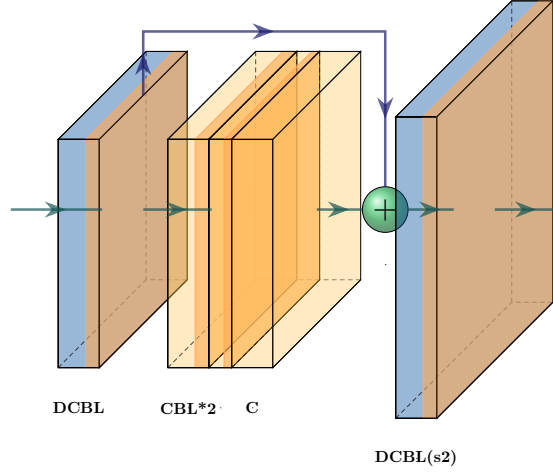


**Fig. 11.** Structure of the decoder block in the generator of ReconGAN/RefineGAN. (C: Convolutional layer; DC: De-Convolutional layer; B: Batch Normalization layer; L: Leaky ReLU layer.)

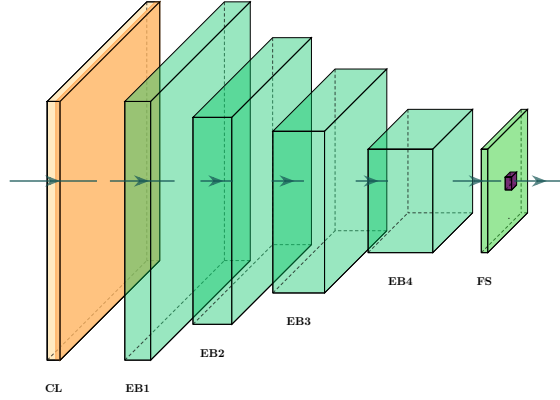


**Fig. 12.** Structure of the discriminator in ReconGAN/RefineGAN. The main structure adopted the encoding path of the generator. A full connection layer and a Sigmoid activation function were cascaded at the end of the discriminator. (C: Convolutional layer; L: Leaky ReLU layer; F: Full Connection layer; S: Sigmoid function; EB: Encoder Block.)

where  $L$  denotes the data range (generally  $L = 1.0$  in MRI reconstruction tasks), and  $N$  is the number of all the pixels in  $I_{\text{rec}}$  and  $I_{\text{gt}}$ . PSNR represents the pixel-wise accuracy of the reconstruction regardless of the acquisition sequences of the multimodal MRI.

Besides, considering the importance of image structural information, such as brightness, contrast and structures, Structural SIMilarity index (SSIM) is formed as:

$$\text{SSIM}(x, y) = \frac{2\mu_x\mu_y + \kappa_1}{\mu_x^2 + \mu_y^2 + \kappa_1} \cdot \frac{\sigma_{xy} + \kappa_2}{\sigma_x^2 + \sigma_y^2 + \kappa_2}, \quad (24)$$

where  $x, y$  denote two images,  $\mu$  and  $\sigma^2$  are the mean and variance,  $\sigma_{xy}$  is the covariance between  $x$  and  $y$ , and  $\kappa_1, \kappa_2$  are constant relaxation terms.

**Perceptual Quality Assessment** The perceptual quality of an image represents how realistic it looks. In MRI images reconstruction tasks, the most reliable perceptual quality assessment is the mean opinion score (MOS), which asks experienced radiologists to rate the reconstructed images. Typically, the images are rated from 0 to 4 depending on the reconstructed image quality (i.e., non-diagnostic, poor, fair, good, and excellent), and the final MOS is calculated as the arithmetic mean of the scores of all raters. In some cases, the rater may also mark the low perceptual quality features such as low SNR and motion artefacts. Although the MOS seems to be faithful, it has limitations such as inter-/inner-raters bias and variance of rating criteria and the scoring might be time-consuming. Thus, the Frechet Inception Distance (FID) [85], as a learning based perceptual quality assessment, is becoming more commonly used for evaluation in GAN based image reconstruction tasks. It considers the high-level global features of a group of images (e.g., the reconstructed images) as a multidimensional Gaussian distribution  $\mathcal{N}(\mu, \Sigma)$ , and measures the differences between the two distributions of the reconstructed images  $\mathbb{I}_{\text{rec}}$  and the ground truth images  $\mathbb{I}_{\text{gt}}$ . It first converts each group of images into a distribution of 2048 features in the latent space of a pre-trained image classification model Inception-V3 [86]. Then, the FID between these two distributions is calculated as:

$$\text{FID}(\mathbb{I}_{\text{rec}}, \mathbb{I}_{\text{gt}}) = \|\mu_{\text{gt}} - \mu_{\text{rec}}\|^2 + \text{Tr}(\Sigma_{\text{gt}} + \Sigma_{\text{rec}} - 2(\Sigma_{\text{gt}}\Sigma_{\text{rec}})^{1/2}). \quad (25)$$

The FID becomes a popular metric for image perceptual quality assessment in GAN based image generation tasks because it is fully automatic and the features extracted from Inception-V3 are close to real-world object classification problems, which tend to mimic human perception similarity for images.

### 3 Benchmarking

In this chapter, we benchmark four GAN based algorithms, i.e., DAGAN, KIGAN, ReconGAN and RefineGAN, for fast MRI. Figure 13 shows the brain reconstruction results using different acceleration factors ( $2\times$ ,  $4\times$ ,  $6\times$ ). It is obvious that the zero-filled (ZF) image has strong artefacts inside the brain tissue. From the entire image, the DAGAN effectively removes the artefacts in the ZF. However, in terms of the zoomed-in areas, there still exists some residual artefacts. For the reconstructions produced by KIGAN, blurring artefacts still exist. Although ReconGAN shows a significant reduction of aliasing artefacts,



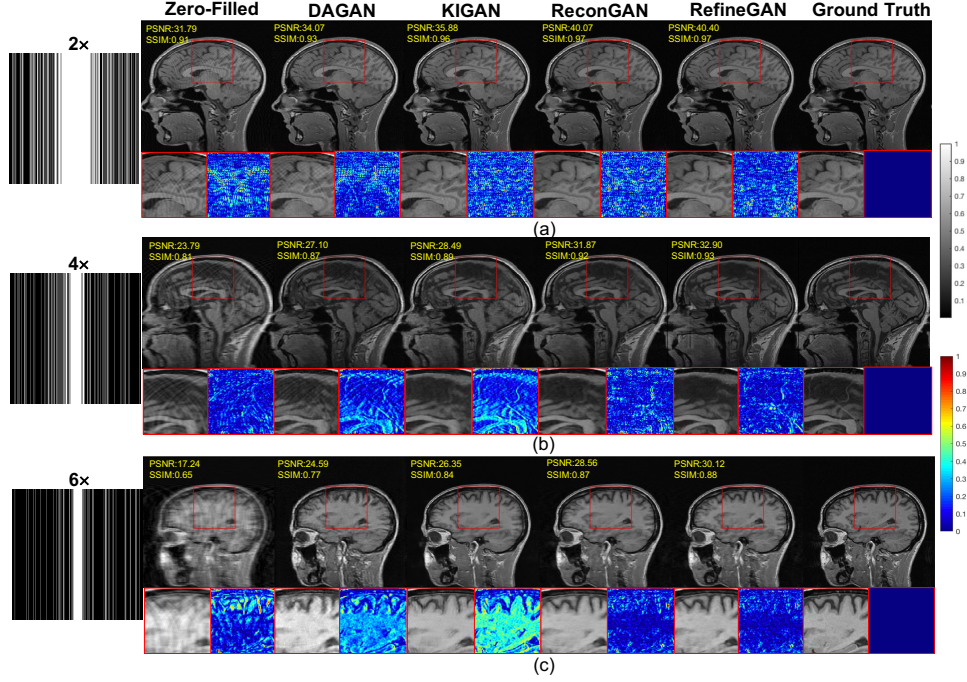


**Fig. 13.** Brain reconstruction result using the Cartesian mask. From top to bottom  $2\times$ ,  $4\times$  and  $6\times$  acceleration, respectively. From left to right are Zero-Filled (ZF), DAGAN, KIGAN, ReconGAN, RefineGAN, Ground Truth (GT).

the edge details are not reconstructed clearly enough. It can be seen that the reconstructed details of RefineGAN are relatively fine, and the reconstruction quality is close to that of the ground truth.

Besides, knee reconstruction results using different Cartesian masks are shown in Figure 14. It can be seen that except for the ZF images, all methods can reconstruct acceptable MR images. As the acceleration factor goes high, obvious aliasing artefacts are produced in DAGAN images. As can be observed in the zoomed-in areas and the corresponding error maps, KIGAN can not restore clear vessels. ReconGAN and RefineGAN show better reconstruction results with higher PSNR and SSIM. In addition, the quantitative values of the RefineGAN are superior to those of the other methods.

Furthermore, we also used radial and spiral masks for training and testing each GAN based method. The sampling rate (SR) of each mask is 50%, 30% and 20%. Figures 15 and 16 show the brain and knee reconstruction results using radial masks. We can see that the image reconstructed by the ZF method under the radial mask has strong blurring artefacts, and the details in the brain and knee cannot be distinguished clearly. When  $SR=20\%$ , from the error maps, we can see that there are still obvious blurring artefacts and obscure blood vessels in

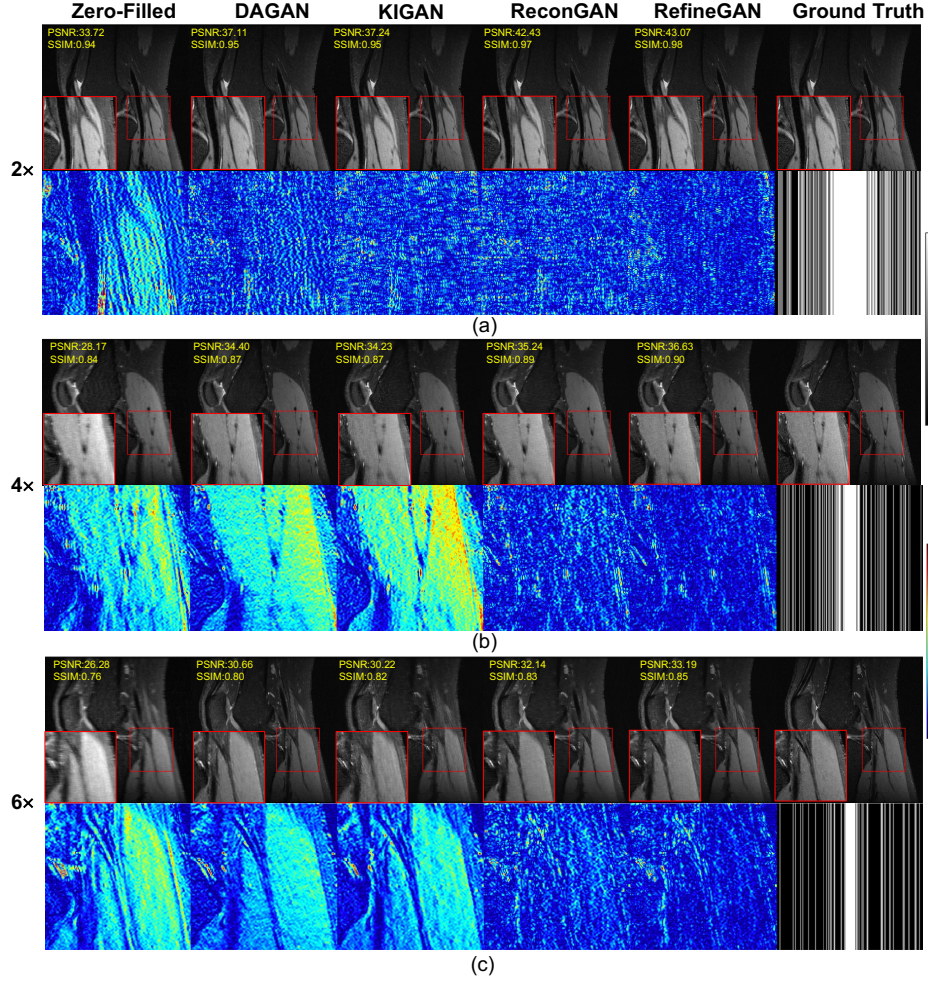


**Fig. 14.** Knee reconstruction result using the Cartesian mask. From top to bottom  $2\times$ ,  $4\times$  and  $6\times$  acceleration, respectively. From left to right are Zero-Filled (ZF), DAGAN, KIGAN, ReconGAN, RefineGAN, Ground Truth (GT).

the results of DAGAN and KIGAN. However, both ReconGAN and RefineGAN can restore sharper vessel edges and finer textures compared to other methods. Besides, RefineGAN has better PSNR and SSIM quantification.

The results are similar using spiral masks. Figures 17 and 18 show the brain and knee reconstruction results of each method using different spiral masks. Through the error map, we can intuitively see that the reconstructed image of RefineGAN has fewer errors, and the reconstruction details are also better. The image reconstructed by RefineGAN can clearly show the details of the gray matter in the brain and the details of the blood vessels in the knee.

**Table 3.** The quantitative metrics (PSNR, SSIM, and RMSE( $\times 10^{-2}$ )) of the brain using different GAN based methods). The bold numbers indicate the best results.

Mask	AF/SR	Metric	ZF	DAGAN	KIGAN	ReconGAN	<b>RefineGAN</b>
Cartesian	2X	PSNR	30.94 $\pm$ 2.75	33.79 $\pm$ 1.88	33.90 $\pm$ 2.55	39.08 $\pm$ 1.34	<b>39.40<math>\pm</math>1.33</b>
		SSIM	0.92 $\pm$ 0.02	0.93 $\pm$ 0.01	0.96 $\pm$ 0.01	<b>0.97<math>\pm</math>0.00</b>	<b>0.97<math>\pm</math>0.00</b>
		RMSE	1.57 $\pm$ 0.01	0.72 $\pm$ 0.43	0.78 $\pm$ 0.53	0.20 $\pm$ 0.09	<b>0.19<math>\pm</math>0.08</b>
	4X	PSNR	23.69 $\pm$ 3.02	28.76 $\pm$ 1.95	28.14 $\pm$ 1.84	32.07 $\pm$ 1.65	<b>32.67<math>\pm</math>1.56</b>
		SSIM	0.79 $\pm$ 0.03	0.86 $\pm$ 0.02	0.88 $\pm$ 0.02	0.92 $\pm$ 0.01	<b>0.93<math>\pm</math>0.01</b>
		RMSE	8.86 $\pm$ 7.01	2.35 $\pm$ 1.50	2.67 $\pm$ 1.40	1.05 $\pm$ 0.54	<b>0.91<math>\pm</math>0.08</b>
	6X	PSNR	19.47 $\pm$ 2.31	25.4 $\pm$ 1.57	27.91 $\pm$ 1.57	29.23 $\pm$ 1.68	<b>29.95<math>\pm</math>1.61</b>
		SSIM	0.66 $\pm$ 0.04	0.77 $\pm$ 0.03	0.86 $\pm$ 0.02	0.88 $\pm$ 0.02	<b>0.89<math>\pm</math>0.02</b>
		RMSE	21.3 $\pm$ 14.1	4.89 $\pm$ 2.33	2.75 $\pm$ 1.31	2.03 $\pm$ 1.00	<b>1.71<math>\pm</math>0.83</b>
	50%	PSNR	34.28 $\pm$ 1.03	35.24 $\pm$ 1.14	38.93 $\pm$ 1.10	37.89 $\pm$ 0.93	<b>39.38<math>\pm</math>0.88</b>
		SSIM	0.87 $\pm$ 0.02	0.91 $\pm$ 0.01	0.96 $\pm$ 0.01	0.95 $\pm$ 0.01	<b>0.97<math>\pm</math>0.00</b>
		RMSE	1.94 $\pm$ 0.22	1.74 $\pm$ 0.22	1.01 $\pm$ 0.12	1.28 $\pm$ 0.13	<b>0.88<math>\pm</math>0.11</b>
Radial	30%	PSNR	28.83 $\pm$ 0.72	30.99 $\pm$ 2.33	33.97 $\pm$ 1.05	34.35 $\pm$ 0.99	<b>35.21<math>\pm</math>1.05</b>
		SSIM	0.73 $\pm$ 0.02	0.82 $\pm$ 0.02	0.91 $\pm$ 0.01	0.91 $\pm$ 0.01	<b>0.92<math>\pm</math>0.01</b>
		RMSE	3.10 $\pm$ 0.30	2.01 $\pm$ 0.27	1.60 $\pm$ 0.18	1.93 $\pm$ 0.21	<b>1.02<math>\pm</math>0.17</b>
	20%	PSNR	26.47 $\pm$ 0.64	28.96 $\pm$ 1.90	31.87 $\pm$ 0.94	31.96 $\pm$ 0.87	<b>32.83<math>\pm</math>0.94</b>
		SSIM	0.65 $\pm$ 0.02	0.78 $\pm$ 0.02	0.84 $\pm$ 0.03	0.87 $\pm$ 0.02	<b>0.89<math>\pm</math>0.02</b>
		RMSE	6.08 $\pm$ 0.36	2.47 $\pm$ 0.45	2.56 $\pm$ 0.27	2.54 $\pm$ 0.25	<b>1.56<math>\pm</math>0.32</b>
	50%	PSNR	34.87 $\pm$ 1.01	38.08 $\pm$ 0.99	41.56 $\pm$ 1.00	43.69 $\pm$ 0.58	<b>44.36<math>\pm</math>0.57</b>
		SSIM	0.90 $\pm$ 0.01	0.95 $\pm$ 0.01	0.96 $\pm$ 0.01	0.97 $\pm$ 0.01	<b>0.98<math>\pm</math>0.00</b>
		RMSE	1.62 $\pm$ 0.18	1.25 $\pm$ 0.01	0.84 $\pm$ 0.10	0.72 $\pm$ 0.66	<b>0.59<math>\pm</math>0.61</b>
	30%	PSNR	29.55 $\pm$ 0.71	34.87 $\pm$ 2.79	36.71 $\pm$ 1.09	37.93 $\pm$ 0.78	<b>38.61<math>\pm</math>0.82</b>
		SSIM	0.83 $\pm$ 0.01	0.87 $\pm$ 0.01	0.91 $\pm$ 0.02	0.95 $\pm$ 0.01	<b>0.95<math>\pm</math>0.00</b>
		RMSE	3.93 $\pm$ 0.28	1.72 $\pm$ 0.41	1.65 $\pm$ 0.20	1.27 $\pm$ 0.11	<b>0.94<math>\pm</math>0.19</b>
Spiral	20%	PSNR	26.62 $\pm$ 0.63	28.87 $\pm$ 2.29	32.43 $\pm$ 0.72	35.02 $\pm$ 0.81	<b>35.11<math>\pm</math>0.85</b>
		SSIM	0.73 $\pm$ 0.01	0.80 $\pm$ 0.04	0.88 $\pm$ 0.03	0.91 $\pm$ 0.01	<b>0.92<math>\pm</math>0.01</b>
		RMSE	7.12 $\pm$ 0.36	2.29 $\pm$ 0.31	2.40 $\pm$ 0.20	1.78 $\pm$ 0.16	<b>1.52<math>\pm</math>0.27</b>

**Table 4.** The quantitative metrics (PSNR, SSIM, and RMSE( $\times 10^{-2}$ )) of the knee using different GAN based methods. The bold numbers indicate the best results.

Mask	AF/SR	Metric	ZF	DAGAN	KIGAN	ReconGAN	RefineGAN
Cartesian	2X	PSNR	34.66 $\pm$ 2.98	38.91 $\pm$ 1.59	38.53 $\pm$ 2.51	42.37 $\pm$ 1.60	<b>42.41<math>\pm</math>1.98</b>
		SSIM	0.95 $\pm$ 0.01	0.94 $\pm$ 0.01	0.96 $\pm$ 0.01	0.97 $\pm$ 0.00	<b>0.98<math>\pm</math>0.00</b>
		RMSE	1.64 $\pm$ 1.32	0.52 $\pm$ 0.31	0.83 $\pm$ 1.03	<b>0.23<math>\pm</math>0.09</b>	0.24 $\pm$ 0.16
	4X	PSNR	27.31 $\pm$ 3.23	34.35 $\pm$ 1.77	34.70 $\pm$ 1.74	34.88 $\pm$ 1.96	<b>35.58<math>\pm</math>1.74</b>
		SSIM	0.84 $\pm$ 0.02	0.86 $\pm$ 0.02	0.89 $\pm$ 0.02	0.90 $\pm$ 0.02	<b>0.91<math>\pm</math>0.02</b>
		RMSE	10.30 $\pm$ 11.00	1.55 $\pm$ 1.20	1.49 $\pm$ 1.27	1.37 $\pm$ 0.93	<b>1.14<math>\pm</math>0.66</b>
	6X	PSNR	25.15 $\pm$ 3.37	32.67 $\pm$ 1.89	30.83 $\pm$ 2.09	32.34 $\pm$ 2.16	<b>33.36<math>\pm</math>1.81</b>
		SSIM	0.79 $\pm$ 0.03	0.82 $\pm$ 0.03	0.84 $\pm$ 0.02	0.86 $\pm$ 0.02	<b>0.87<math>\pm</math>0.02</b>
		RMSE	18.2 $\pm$ 22.3	2.36 $\pm$ 2.09	4.08 $\pm$ 4.29	2.62 $\pm$ 2.19	<b>2.00<math>\pm</math>1.52</b>
	50%	PSNR	35.17 $\pm$ 1.37	36.70 $\pm$ 1.37	37.17 $\pm$ 1.37	38.38 $\pm$ 1.22	<b>38.91<math>\pm</math>1.21</b>
		SSIM	0.90 $\pm$ 0.02	0.91 $\pm$ 0.01	0.92 $\pm$ 0.01	<b>0.93<math>\pm</math>0.01</b>	<b>0.93<math>\pm</math>0.01</b>
		RMSE	2.37 $\pm$ 0.50	1.97 $\pm$ 0.59	1.53 $\pm$ 0.18	1.22 $\pm$ 0.16	<b>1.14<math>\pm</math>0.15</b>
Radial	30%	PSNR	32.69 $\pm$ 1.13	34.02 $\pm$ 1.39	35.27 $\pm$ 1.40	35.96 $\pm$ 1.27	<b>36.21<math>\pm</math>1.29</b>
		SSIM	0.80 $\pm$ 0.03	0.87 $\pm$ 0.02	0.88 $\pm$ 0.01	0.88 $\pm$ 0.02	<b>0.89<math>\pm</math>0.02</b>
		RMSE	4.87 $\pm$ 0.89	2.23 $\pm$ 0.76	1.39 $\pm$ 0.67	1.61 $\pm$ 0.22	<b>1.36<math>\pm</math>0.32</b>
	20%	PSNR	30.77 $\pm$ 1.15	33.69 $\pm$ 1.51	33.49 $\pm$ 1.54	34.48 $\pm$ 1.26	<b>34.72<math>\pm</math>1.30</b>
		SSIM	0.75 $\pm$ 0.03	0.84 $\pm$ 0.02	0.85 $\pm$ 0.02	<b>0.86<math>\pm</math>0.02</b>	<b>0.86<math>\pm</math>0.02</b>
		RMSE	7.13 $\pm$ 1.24	2.76 $\pm$ 0.87	2.68 $\pm$ 0.73	1.91 $\pm$ 0.27	<b>1.61<math>\pm</math>0.34</b>
	50%	PSNR	35.62 $\pm$ 1.27	39.37 $\pm$ 1.39	41.39 $\pm$ 1.37	42.53 $\pm$ 0.75	<b>43.04<math>\pm</math>0.77</b>
		SSIM	0.91 $\pm$ 0.02	0.94 $\pm$ 0.01	0.94 $\pm$ 0.02	0.96 $\pm$ 0.01	<b>0.97<math>\pm</math>0.02</b>
		RMSE	1.78 $\pm$ 0.54	1.06 $\pm$ 0.10	0.97 $\pm$ 0.14	0.73 $\pm$ 0.15	<b>0.61<math>\pm</math>0.07</b>
Spiral	30%	PSNR	33.48 $\pm$ 1.12	36.19 $\pm$ 1.35	36.26 $\pm$ 1.18	38.20 $\pm$ 1.31	<b>38.49<math>\pm</math>1.33</b>
		SSIM	0.86 $\pm$ 0.02	0.90 $\pm$ 0.01	0.90 $\pm$ 0.02	<b>0.92<math>\pm</math>0.01</b>	<b>0.92<math>\pm</math>0.01</b>
		RMSE	3.71 $\pm$ 0.91	1.67 $\pm$ 0.72	1.64 $\pm$ 0.35	1.24 $\pm$ 0.18	<b>0.98<math>\pm</math>0.23</b>
	20%	PSNR	30.97 $\pm$ 1.14	34.88 $\pm$ 1.39	33.83 $\pm$ 1.50	36.51 $\pm$ 1.23	<b>36.75<math>\pm</math>1.27</b>
		SSIM	0.81 $\pm$ 0.03	0.88 $\pm$ 0.02	0.88 $\pm$ 0.01	<b>0.90<math>\pm</math>0.02</b>	<b>0.90<math>\pm</math>0.02</b>
		RMSE	5.39 $\pm$ 1.26	2.29 $\pm$ 0.56	1.95 $\pm$ 0.25	1.51 $\pm$ 0.20	<b>1.32<math>\pm</math>0.14</b>

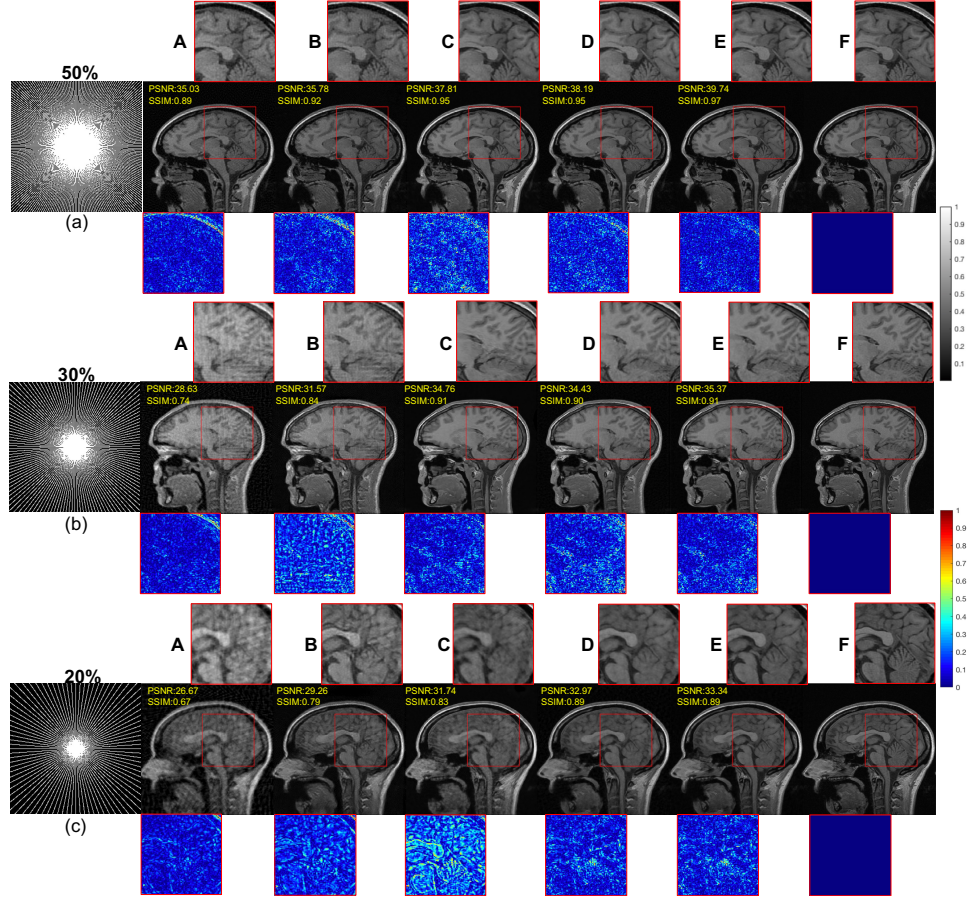


**Fig. 15.** Brain reconstruction result using the radial mask. From top to bottom, the sampling rate (SR) is 50%, 30%, and 20%, respectively. From left to right are Zero-Filled (ZF), DAGAN, KIGAN, ReconGAN, RefineGAN, Ground Truth (GT).

The quantitative metrics (PSNR, SSIM and RMSE) of each GAN based method using different under-sampling masks are shown in Tables 3 and 4. We can draw similar conclusions as the qualitative visualisation results that the image quality after RefineGAN reconstruction is better than other methods. Even at a high acceleration factor or high under-sampling rate, the reconstructed images of RefineGAN still have high SNR.

Tables 3 and 4 show the quantitative metrics, including PSNR, SSIM and RMSE for all compared methods. The numbers in Tables 3 and 4 represent the mean and standard deviation values of the corresponding metrics (bold numbers indicate the best performance). Compared to DAGAN, KIGAN and ReconGAN, the RefineGAN framework has outperformed them remarkably at different acceleration factors.



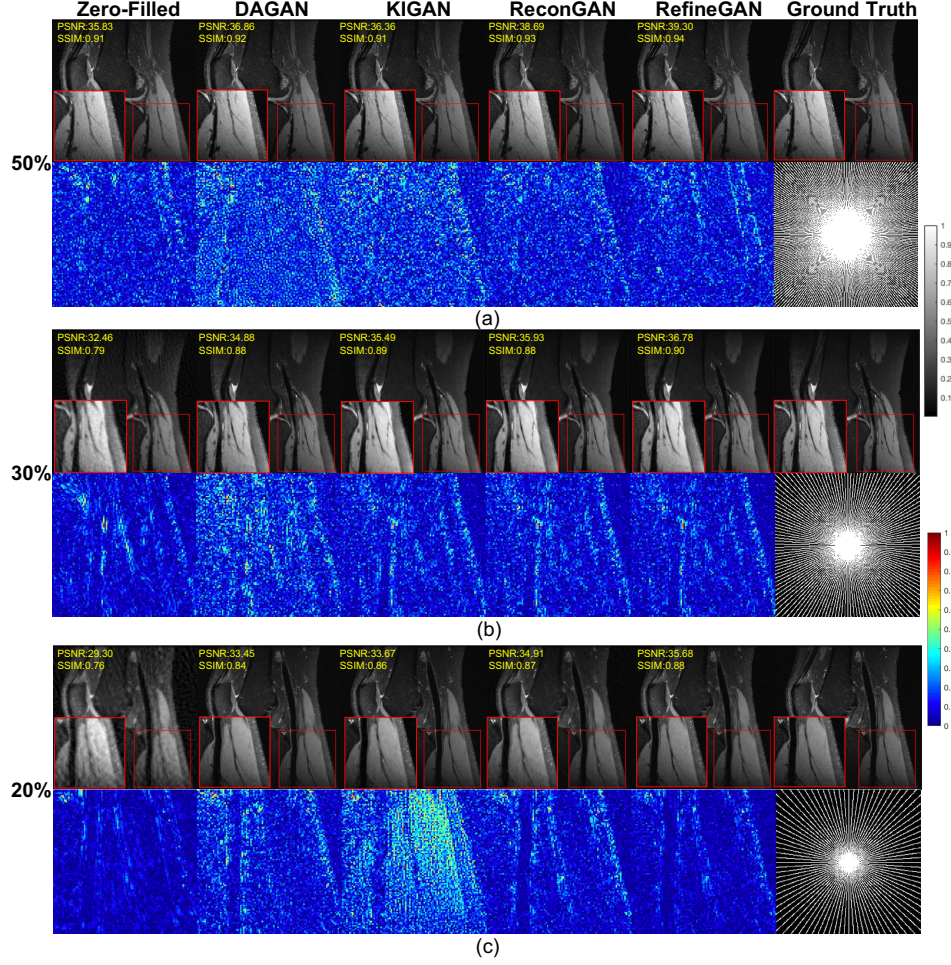


**Fig. 16.** Knee reconstruction result using the radial mask. From top to bottom  $2\times$ ,  $4\times$  and  $6\times$  acceleration, respectively. From left to right are Zero-Filled (ZF), DAGAN, KIGAN, ReconGAN, RefineGAN, Ground Truth (GT).

## 4 Discussion

We have established that GAN based methods such as DAGAN, KIGAN, ReconGAN, and RefineGAN excel in generating faithful, photo-realistic reconstruction of undersampled MR images and in removing the undersampling artefacts. Despite their representing a successful category of CS-MRI techniques, GAN based methods suffer from training instability and slow convergence to a global minimum [87,88]. This problem can be alleviated by Wasserstein GAN (WGAN) [89]. Instead of minimising Jensen-Shannon divergence between the

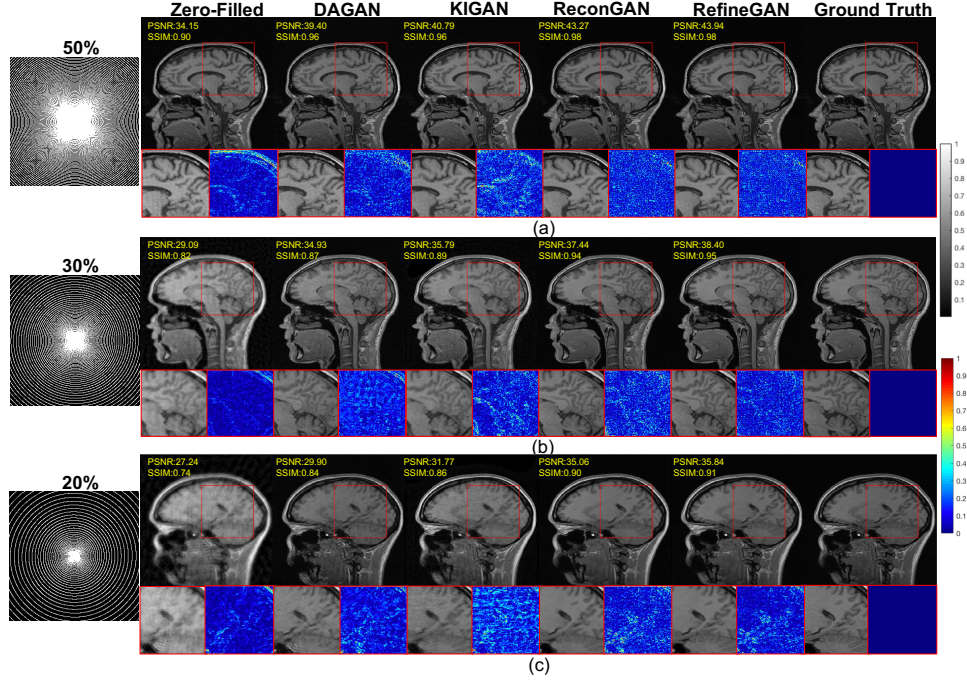


**Fig. 17.** Brain reconstruction result using the radial mask. From top to bottom, the sampling rate (SR) is 50%, 30%, and 20%, respectively. From left to right are Zero-Filled (ZF), DAGAN, KIGAN, ReconGAN, RefineGAN, Ground Truth (GT).

reconstructed image and ground truth in the training phase, WGAN aims to reduce the Wasserstein distance. WGAN based CS-MRI models have achieved superior reconstruction performance compared with GAN based methods e.g., DAGAN [90,91]. However, to minimise the Wasserstein distance, the discriminator needs to satisfy the 1-Lipschitz constraint. The original WGAN paper adopted a weight clipping approach to enforce this constraint but this can itself cause training instability. The potential improvement includes a gradient clipping approach [92] or dividing the weights of neural networks by their spectral norm [93]. Altogether, modifying the loss function of GAN is key to addressing its training instability issue.

Another problem with the GAN loss function is that it may affect the high frequency texture [63] and smoothing the reconstructed image [94]. GAN may also generate high frequency noise [63]. Mardani et al. (2019) suggested solving the high frequency texture issue with the least square GAN [63]. L1 loss between reconstructed images and ground truth was also added as an auxiliary function, to serve as a low-pass filter to remove high frequency noises.

Apart from the issues with the GAN loss function during training, GAN based methods suffer from reconstruction instability [95]. This means that a small per-



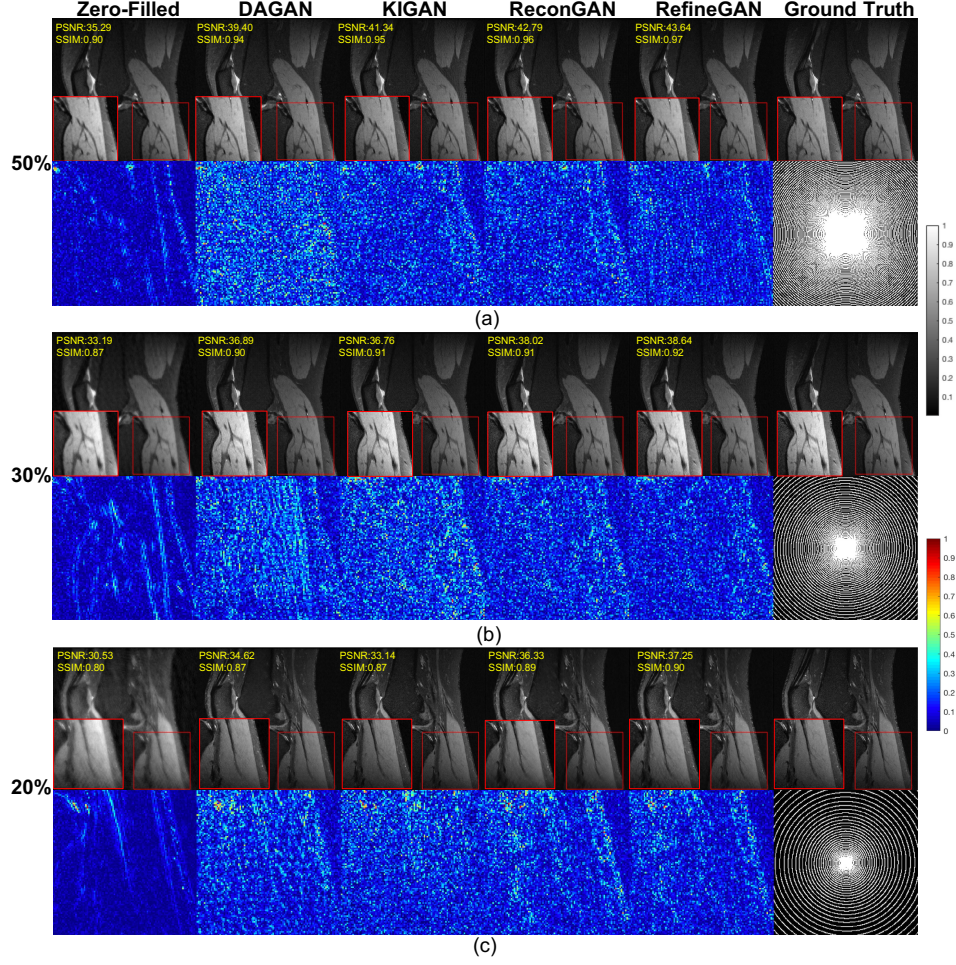


**Fig. 18.** Knee reconstruction result using the radial mask. From top to bottom  $2\times$ ,  $4\times$  and  $6\times$  acceleration, respectively. From left to right are Zero-Filled (ZF), DAGAN, KIGAN, ReconGAN, RefineGAN, Ground Truth (GT).

turbation to the input image leads to large scale changes in the reconstruction output. Antun et al. (2020) [95] evaluated the instabilities of DAGAN and other deep learning based CS-MRI models and showed that the performance of DAGAN deteriorated as the undersampling ratio increased during testing. That is if more  $k$ -space pixels were undersampled more than the undersampling ratio in the images used to train DAGAN, its performance decreases. In contrast, variational network and deep cascaded convolutional neural networks (DC-CNN), two non-GAN based techniques, did not experience the same issue. This indicates the incorporation of GAN may reduce the generalisability of the model



to images collected under different undersampling ratios and contribute to its reconstruction instability.

Another instability issue with DAGAN is that if small structural details were added to an MRI image, such as random letters, and this image was undersampled retrospectively, DAGAN was unable to reconstruct the structural details. In contrast, variational network and DC-CNN were superior in recovering these structural details [95]. Even though these two instability tests revealed a critical weakness of DAGAN, DAGAN, being one of the earliest GAN based methods, may not capture the improved reconstruction accuracy and network architectural complexity of the more recent methods [90,91]. Hence, more instability testing is required on more GAN based methods to conclude whether this category of CS-MRI techniques suffers from reconstruction instability.

These results on instability testing still question the generalisability of GAN based models. In other words, it is unclear whether after being trained with images from one source, e.g., one organ, under one undersampling ratio etc, a model will achieve equivalent performance on images from another source. This is often referred to in the literature as a zero-shot inference test. However, GAN based methods appear to excel in these inference tests. To illustrate, DAGAN, having been trained with MR images of the brain of a healthy volunteer, successfully reconstructed the MR images from a patient with the brain tumour, faithfully preserving the tumour structure [3]. Another example is that GANCS, another GAN based method, was trained with MR images of the abdomen and any images containing the enlarged adrenal gland were removed from the training set. In testing, GANCS was capable of recovering enlarged adrenal gland in patients with adrenal hypertrophy. No evidence of hallucination of the reconstructed images was found [63]. These successes in the zero-shot inference of pathological structures challenged the instability test results from Antun et al. One interpretation is that the additional structural details added to the MR images by Antun et al., such as letters, may not represent real-life physiological or pathological deviations of the MR images from the training set. It was also possible that the zero-shot inference tests on DAGAN and GANCS concerned only a small sample size, limited to a few pathological conditions. Larger scale zero-shot inference tests are necessary to evaluate the generalisability of GAN based CS-MRI methods.

In summary, future research directions on GAN based fast MRI may include more robust training strategies, e.g., combining GAN with genetic algorithm [96], incorporating edge and texture enhancement [54], reducing possible hallucination [97,98], coupling with explainable AI (XAI) modules [99,100], and further consideration with MR physics [55].

## 5 Conclusion

We carried out a mini review, benchmarked and compared four different GAN-based network architectures for fast MRI reconstruction in this chapter. Our comparison used the various sampling patterns, different masks on corresponding

datasets that have covered commonly used clinical MRI scenarios. For our systematic research and measurement, we used both traditional and newly proposed quantitative tools. The outcomes of qualitative visualization were also examined and compared. To summarise, our mini review and benchmarking have revealed that all GAN-based approaches could obtain promising results at lower acceleration factors. However, when the acceleration factors are high, some GAN-based architectures, such as DAGAN and KIGAN, may not be sufficient for MRI reconstruction applications. Furthermore, as compared to other GAN-based methods, the RefineGAN has improved reconstruction accuracy and perceptual efficiency. Future development incorporating MR physics and XAI into GAN based models will provide promising pathways for clinical deployment with more transparency of the reconstruction algorithms.

## References

1. Kieren Grant Hollingsworth. Reducing acquisition time in clinical MRI by data undersampling and compressed sensing reconstruction. *Phys. Med. Biol.*, pages R297–322, 2015.
2. Michael Lustig, David Donoho, and John M. Pauly. Sparse MRI: The application of compressed sensing for rapid MR imaging. *Magnetic Resonance in Medicine*, 58(6):1182–1195, dec 2007.
3. Guang Yang, Simiao Yu, Hao Dong, Greg Slabaugh, Pier Luigi Dragotti, Xujiong Ye, Fangde Liu, Simon Arridge, Jennifer Keegan, Yike Guo, and David Firmin. DAGAN: Deep De-Aliasing Generative Adversarial Networks for Fast Compressed Sensing MRI Reconstruction. *IEEE Transactions on Medical Imaging*, 37(6):1310–1321, jun 2018.
4. Paul Suetens. *Fundamentals of Medical Imaging*. Cambridge University Press, 2nd edition, 2009.
5. P Mansfield. Multi-planar image formation using NMR spin echoes. *Journal of Physics C: Solid State Physics*, 1977.
6. J. Hennig, A. Nauerth, and H. Friedburg. RARE imaging: A fast imaging method for clinical MR. *Magnetic Resonance in Medicine*, 3(6):823–833, 1986.
7. A Haase, J Frahm, D Matthaei, and K.-D Merboldt. FLASH Imaging. Rapid NMR Imaging Using Low Flip-Angle Pulses. Technical report, 1986.
8. E. Zisselman, A. Adler, and M. Elad. Compressed Learning for Image Classification: A Deep Neural Network Approach. In *Handbook of Numerical Analysis*, volume 19, pages 3–17. Elsevier B.V., jan 2018.
9. Merlin J. Fair, Peter D. Gatehouse, Edward V.R. DiBella, and David N. Firmin. A review of 3D first-pass, whole-heart, myocardial perfusion cardiovascular magnetic resonance, aug 2015.
10. Saiprasad Ravishankar and Yoram Bresler. MR image reconstruction from highly undersampled k-space data by dictionary learning. *IEEE Transactions on Medical Imaging*, 30(5):1028–1041, may 2011.
11. Junfeng Yang, Yin Zhang, and Wotao Yin. A fast alternating direction method for TVL1-L2 signal reconstruction from partial Fourier data. *IEEE Journal on Selected Topics in Signal Processing*, 4(2):288–297, apr 2010.
12. Ender M. Eksioğlu. Decoupled Algorithm for MRI Reconstruction Using Nonlocal Block Matching Model: BM3D-MRI. *Journal of Mathematical Imaging and Vision*, 56(3):430–440, nov 2016.
13. Yue Hu, Greg Ongie, Sathish Ramani, and Mathews Jacob. Generalized higher degree total variation (HDTV) regularization. *IEEE Transactions on Image Processing*, 23(6):2423–2435, 2014.
14. Yunsong Liu, Jian-Feng Cai, Zhifang Zhan, Di Guo, Jing Ye, Zhong Chen, and Xiaobo Qu. Balanced Sparse Model for Tight Frames in Compressed Sensing Magnetic Resonance Imaging. *PLOS ONE*, 10(4):e0119584, apr 2015.
15. Mohammad H. Kayvanrad, A. Jonathan McLeod, John S.H. Baxter, Charles A. McKenzie, and Terry M. Peters. Stationary wavelet transform for under-sampled MRI reconstruction. *Magnetic Resonance Imaging*, 32(10):1353–1364, dec 2014.
16. M. Guerquin-Kern, M. Haberland, K. P. Pruessmann, and M. Unser. A fast wavelet-based reconstruction method for magnetic resonance imaging. *IEEE Transactions on Medical Imaging*, 30(9):1649–1660, sep 2011.
17. Kerstin Hammernik, Teresa Klatzer, Erich Kobler, Michael P. Recht, Daniel K. Sodickson, Thomas Pock, and Florian Knoll. Learning a variational network

- for reconstruction of accelerated MRI data. *Magnetic Resonance in Medicine*, 79(6):3055–3071, jun 2018.
18. Jun Chen, Guang Yang, Habib Khan, Heye Zhang, Yanping Zhang, Shu Zhao, Raad Mohiaddin, Tom Wong, David Firmin, and Jennifer Keegan. JAS-GAN: Generative adversarial network based joint atrium and scar segmentation on unbalanced atrial targets. *IEEE Journal of Biomedical and Health Informatics*.
  19. Yinzhe Wu, Suzan Hatipoglu, Diego Alonso-Álvarez, Peter Gatehouse, Binghuan Li, Yikai Gao, David Firmin, Jennifer Keegan, and Guang Yang. Fast and automated segmentation for the three-directional multi-slice cine myocardial velocity mapping. *Diagnostics*, 11(2):346, 2021.
  20. Yinzhe Wu, Suzan Hatipoglu, Diego Alonso-Álvarez, Peter Gatehouse, David Firmin, Jennifer Keegan, and Guang Yang. Automated multi-channel segmentation for the 4D myocardial velocity mapping cardiac mr. In *Medical Imaging 2021: Computer-Aided Diagnosis*, volume 11597, page 115970P. International Society for Optics and Photonics, 2021.
  21. Yao Jin, Guang Yang, Ying Fang, Ruipeng Li, Xiaomei Xu, Yongkai Liu, and Xiaobo Lai. 3D PBV-Net: an automated prostate MRI data segmentation method. *Computers in Biology and Medicine*, 128:104160, 2021.
  22. Xi Zhou, Qinghao Ye, Yinghui Jiang, Minhao Wang, Zhangming Niu, Wade Menpes-Smith, Evandro Fei Fang, Zhi Liu, Jun Xia, and Guang Yang. Systematic and comprehensive automated ventricle segmentation on ventricle images of the elderly patients: A retrospective study. *Frontiers in Aging Neuroscience*, 12, 2020.
  23. Yongkai Liu, Guang Yang, Melina Hosseiny, Afshin Azadikhah, Sohrab Afshari Mirak, Qi Miao, Steven S Raman, and Kyunghyun Sung. Exploring uncertainty measures in bayesian deep attentive neural networks for prostate zonal segmentation. *IEEE Access*, 8:151817–151828, 2020.
  24. Pedro F Ferreira, Raquel R Martin, Andrew D Scott, Zohya Khaliq, Guang Yang, Sonia Nielles-Vallespin, Dudley J Pennell, and David N Firmin. Automating in vivo cardiac diffusion tensor postprocessing with deep learning-based segmentation. *Magnetic resonance in medicine*, 84(5):2801–2814, 2020.
  25. Ming Li, Chengjia Wang, Heye Zhang, and Guang Yang. Mv-ran: Multiview recurrent aggregation network for echocardiographic sequences segmentation and full cardiac cycle analysis. *Computers in biology and medicine*, 120:103728, 2020.
  26. Yongkai Liu, Guang Yang, Sohrab Afshari Mirak, Melina Hosseiny, Afshin Azadikhah, Xinran Zhong, Robert E Reiter, Yeejin Lee, Steven S Raman, and Kyunghyun Sung. Automatic prostate zonal segmentation using fully convolutional network with feature pyramid attention. *IEEE Access*, 7:163626–163632, 2019.
  27. Xiahai Zhuang, Lei Li, Christian Payer, Darko Štern, Martin Urschler, Mattias P Heinrich, Julien Oster, Chunliang Wang, Örjan Smedby, Cheng Bian, et al. Evaluation of algorithms for multi-modality whole heart segmentation: an open-access grand challenge. *Medical image analysis*, 58:101537, 2019.
  28. Yuanhan Mo, Fangde Liu, Douglas McIlwraith, Guang Yang, Jingqing Zhang, Taigang He, and Yike Guo. The deep poincaré map: A novel approach for left ventricle segmentation. In *International Conference on Medical Image Computing and Computer-Assisted Intervention*, pages 561–568. Springer, 2018.
  29. Wenbo Zhang, Guang Yang, He Huang, Weiji Yang, Xiaomei Xu, Yongkai Liu, and Xiaobo Lai. ME-Net: Multi-encoder net framework for brain tumor segmentation. *International Journal of Imaging Systems and Technology*, 2021.

30. Guang Yang, Jun Chen, Zhifan Gao, Shuo Li, Hao Ni, Elsa Angelini, Tom Wong, Raad Mohiaddin, Eva Nyktari, Ricardo Wage, et al. Simultaneous left atrium anatomy and scar segmentations via deep learning in multiview information with attention. *Future Generation Computer Systems*, 107:215–228, 2020.
31. Lei Li, Fuping Wu, Guang Yang, Lingchao Xu, Tom Wong, Raad Mohiaddin, David Firmin, Jennifer Keegan, and Xiahai Zhuang. Atrial scar quantification via multi-scale cnn in the graph-cuts framework. *Medical image analysis*, 60:101595, 2020.
32. Lei Zhang, Guang Yang, and Xujiong Ye. Automatic skin lesion segmentation by coupling deep fully convolutional networks and shallow network with textons. *Journal of Medical Imaging*, 6(2):024001, 2019.
33. Guang Yang, Xiahai Zhuang, Habib Khan, Eva Nyktari, Shouvik Haldar, Lei Li, Rick Wage, Xujiong Ye, Greg Slabaugh, Raad Mohiaddin, et al. Left atrial scarring segmentation from delayed-enhancement cardiac MRI images: A deep learning approach. *Cardiovascular Imaging and Image Analysis*, page 109, 2018.
34. Spyridon Bakas, Mauricio Reyes, Andras Jakab, Stefan Bauer, Markus Rempfler, Alessandro Crimi, Russell Takeshi Shinohara, Christoph Berger, Sung Min Ha, Martin Rozycki, et al. Identifying the best machine learning algorithms for brain tumor segmentation, progression assessment, and overall survival prediction in the brats challenge. *arXiv preprint arXiv:1811.02629*, 2018.
35. Tony CW Mok and Albert Chung. Fast symmetric diffeomorphic image registration with convolutional neural networks. In *Proceedings of the IEEE/CVF conference on computer vision and pattern recognition*, pages 4644–4653, 2020.
36. Bob D de Vos, Floris F Berendsen, Max A Viergever, Marius Staring, and Ivana Išgum. End-to-end unsupervised deformable image registration with a convolutional neural network. In *Deep learning in medical image analysis and multimodal learning for clinical decision support*, pages 204–212. Springer, 2017.
37. Guorong Wu, Minjeong Kim, Qian Wang, Brent C Munsell, and Dinggang Shen. Scalable high-performance image registration framework by unsupervised deep feature representations learning. *IEEE Transactions on Biomedical Engineering*, 63(7):1505–1516, 2015.
38. Chenchu Xu, Dong Zhang, Jaron Chong, Bo Chen, and Shuo Li. Synthesis of gadolinium-enhanced liver tumors on nonenhanced liver MR images using pixel-level graph reinforcement learning. *Medical Image Analysis*, 69:101976, 2021.
39. Chengjia Wang, Guang Yang, Giorgos Papanastasiou, Sotirios A Tsaftaris, David E Newby, Calum Gray, Gillian Macnaught, and Tom J MacGillivray. Di-Cyc: GAN-based deformation invariant cross-domain information fusion for medical image synthesis. *Information Fusion*, 67:147–160, 2021.
40. Zhifan Gao, Heye Zhang, Shizhou Dong, Shanhui Sun, Xin Wang, Guang Yang, Wanqing Wu, Shuo Li, and Victor Hugo C de Albuquerque. Salient object detection in the distributed cloud-edge intelligent network. *IEEE Network*, 34(2):216–224, 2020.
41. Chengjia Wang, Shizhou Dong, Xiaofeng Zhao, Giorgos Papanastasiou, Heye Zhang, and Guang Yang. Saliencygan: Deep learning semisupervised salient object detection in the fog of iot. *IEEE Transactions on Industrial Informatics*, 16(4):2667–2676, 2019.
42. Abder-Rahman Ali, Jingpeng Li, Summrina Kanwal, Guang Yang, Amir Hussain, and Sally Jane O’Shea. A novel fuzzy multilayer perceptron (F-MLP) for the detection of irregularity in skin lesion border using dermoscopic images. *Frontiers in medicine*, 7, 2020.

43. Meijun Yang, Xiaoyan Xiao, Zhi Liu, Longkun Sun, Wei Guo, Lizhen Cui, Dianmin Sun, Pengfei Zhang, and Guang Yang. Deep retinanet for dynamic left ventricle detection in multiview echocardiography classification. *Scientific Programming*, 2020, 2020.
44. Min Li, Shizhong Dong, Kun Zhang, Zhifan Gao, Xi Wu, Heye Zhang, Guang Yang, and Shuo Li. Deep learning intra-image and inter-images features for co-saliency detection. In *BMVC*, volume 291, 2018.
45. Shizhong Dong, Zhifan Gao, Shanhui Sun, Xin Wang, Ming Li, Heye Zhang, Guang Yang, Huafeng Liu, Shuo Li, et al. Holistic and deep feature pyramids for saliency detection. In *BMVC*, page 67, 2018.
46. Hao Dong, Guang Yang, Fangde Liu, Yuanhan Mo, and Yike Guo. Automatic brain tumor detection and segmentation using U-Net based fully convolutional networks. In *annual conference on medical image understanding and analysis*, pages 506–517. Springer, 2017.
47. Shaoping Hu, Yuan Gao, Zhangming Niu, Yinghui Jiang, Lao Li, Xianglu Xiao, Minhao Wang, Evandro Fei Fang, Wade Menpes-Smith, Jun Xia, et al. Weakly supervised deep learning for COVID-19 infection detection and classification from ct images. *IEEE Access*, 8:118869–118883, 2020.
48. Yankun Cao, Ziqiao Wang, Zhi Liu, Yujun Li, Xiaoyan Xiao, Longkun Sun, Yang Zhang, Haixia Hou, Pengfei Zhang, and Guang Yang. Multiparameter synchronous measurement with IVUS images for intelligently diagnosing coronary cardiac disease. *IEEE Transactions on Instrumentation and Measurement*, 2020.
49. Nan Zhang, Guang Yang, Zhifan Gao, Chenchu Xu, Yanping Zhang, Rui Shi, Jennifer Keegan, Lei Xu, Heye Zhang, Zhanming Fan, et al. Deep learning for diagnosis of chronic myocardial infarction on nonenhanced cardiac cine MRI. *Radiology*, 291(3):606–617, 2019.
50. Michael Roberts, Derek Driggs, Matthew Thorpe, Julian Gilbey, Michael Yeung, Stephan Ursprung, Angelica I Aviles-Rivero, Christian Etmann, Cathal McCague, Lucian Beer, et al. Machine learning for COVID-19 detection and prognostication using chest radiographs and CT scans: a systematic methodological review. *arXiv preprint arXiv:2008.06388*, 2020.
51. Mohammadreza Soltaninejad, Lei Zhang, Tryphon Lambrou, Guang Yang, Nigel Allinson, and Xujiong Ye. MRI brain tumor segmentation and patient survival prediction using random forests and fully convolutional networks. In *International MICCAI Brainlesion Workshop*, pages 204–215. Springer, 2017.
52. Cheng Jin, Heng Yu, Jia Ke, Peirong Ding, Yongju Yi, Xiaofeng Jiang, Xin Duan, Jinghua Tang, Daniel T Chang, Xiaojian Wu, et al. Predicting treatment response from longitudinal images using multi-task deep learning. *Nature communications*, 12(1):1–11, 2021.
53. Anne Nielsen, Mikkel Bo Hansen, Anna Tietze, and Kim Mouridsen. Prediction of tissue outcome and assessment of treatment effect in acute ischemic stroke using deep learning. *Stroke*, 49(6):1394–1401, 2018.
54. Yutong Chen, David Firmin, and Guang Yang. Wavelet improved GAN for MRI reconstruction. In *Medical Imaging 2021: Physics of Medical Imaging*, volume 11595, page 1159513. International Society for Optics and Photonics, 2021.
55. Jun Lv, Chengyan Wang, and Guang Yang. Pic-gan: A parallel imaging coupled generative adversarial network for accelerated multi-channel mri reconstruction. *Diagnostics*, 11(1):61, 2021.
56. J Lv, J Zhu, and G Yang. Which GAN? a comparative study of generative adversarial network (GAN) based fast MRI reconstruction. *Philosophical Transactions of the Royal Society A*.

57. Zhenmou Yuan, Mingfeng Jiang, Yaming Wang, Bo Wei, Yongming Li, Pin Wang, Wade Menpes-Smith, Zhangming Niu, and Guang Yang. SARA-GAN: Self-attention and relative average discriminator based generative adversarial networks for fast compressed sensing MRI reconstruction. *Frontiers in Neuroinformatics*, 14, 2020.
58. Yifeng Guo, Chengjia Wang, Heye Zhang, and Guang Yang. Deep attentive wasserstein generative adversarial networks for mri reconstruction with recurrent context-awareness. In *International Conference on Medical Image Computing and Computer-Assisted Intervention*, pages 167–177. Springer, 2020.
59. Jo Schlemper, Guang Yang, Pedro Ferreira, Andrew Scott, Laura-Ann McGill, Zohya Khalique, Margarita Gorodezky, Malte Roehl, Jennifer Keegan, Dudley Pennell, et al. Stochastic deep compressive sensing for the reconstruction of diffusion tensor cardiac MRI. In *International conference on medical image computing and computer-assisted intervention*, pages 295–303. Springer, 2018.
60. Maximilian Seitzer, Guang Yang, Jo Schlemper, Ozan Oktay, Tobias Würfl, Vincent Christlein, Tom Wong, Raad Mohiaddin, David Firmin, Jennifer Keegan, et al. Adversarial and perceptual refinement for compressed sensing mri reconstruction. In *International conference on medical image computing and computer-assisted intervention*, pages 232–240. Springer, 2018.
61. David L Donoho et al. Compressed sensing. *IEEE Transactions on information theory*, 52(4):1289–1306, 2006.
62. Tran Minh Quan, Thanh Nguyen-Duc, and Won Ki Jeong. Compressed Sensing MRI Reconstruction Using a Generative Adversarial Network With a Cyclic Loss. *IEEE Transactions on Medical Imaging*, 37(6):1488–1497, jun 2018.
63. Morteza Mardani, Enhao Gong, Joseph Y. Cheng, Shreyas S. Vasanawala, Greg Zaharchuk, Lei Xing, and John M. Pauly. Deep generative adversarial neural networks for compressive sensing MRI. *IEEE Transactions on Medical Imaging*, 38(1):167–179, jan 2019.
64. Jo Schlemper, Jose Caballero, Joseph V. Hajnal, Anthony N. Price, and Daniel Rueckert. A Deep Cascade of Convolutional Neural Networks for Dynamic MR Image Reconstruction. *IEEE Transactions on Medical Imaging*, 37(2):491–503, feb 2018.
65. Qiaoying Huang, Dong Yang, Pengxiang Wu, Hui Qu, Jingru Yi, and Dimitris Metaxas. MRI reconstruction via cascaded channel-wise attention network. In *Proceedings - International Symposium on Biomedical Imaging*, volume 2019-April, pages 1622–1626. IEEE Computer Society, apr 2019.
66. Taejoon Eo, Yohan Jun, Taeseong Kim, Jinseong Jang, Ho-Joon Lee, and Dosik Hwang. KIKI-net: cross-domain convolutional neural networks for reconstructing undersampled magnetic resonance images. *Magnetic Resonance in Medicine*, 80(5):2188–2201, nov 2018.
67. Simiao Yu, Hao Dong, Guang Yang, Greg Slabaugh, Pier Luigi Dragotti, Xujiang Ye, Fangde Liu, Simon Arridge, Jennifer Keegan, David Firmin, et al. Deep de-aliasing for fast compressive sensing MRI. *arXiv preprint arXiv:1705.07137*, 2017.
68. Ian J Goodfellow, Jean Pouget-Abadie, Mehdi Mirza, Bing Xu, David Warde-Farley, Sherjil Ozair, Aaron Courville, and Yoshua Bengio. Generative Adversarial Nets. Technical report, 2014.
69. Xin Deng, Ren Yang, Eth Zurich, Mai Xu, and Pier Luigi Dragotti. Wavelet Domain Style Transfer for an Effective Perception-distortion Tradeoff in Single Image Super-Resolution. Technical report, 2019.

70. Anagha Deshmane, Vikas Gulani, Mark A. Griswold, and Nicole Seiberlich. Parallel MR imaging. *Journal of Magnetic Resonance Imaging*, 36(1):55–72, 2012. eprint: <https://onlinelibrary.wiley.com/doi/pdf/10.1002/jmri.23639>.
71. Xiaohua Zhang, Qiusheng Lian, Yuchi Yang, and Yueming Su. A deep unrolling network inspired by total variation for compressed sensing MRI. *Digital Signal Processing: A Review Journal*, 107, 2020. Publisher: Elsevier.
72. Steven Diamond, Vincent Sitzmann, Felix Heide, and Gordon Wetzstein. Unrolled Optimization with Deep Priors. *arXiv*, 2017. Publisher: arxiv.org.
73. Chen Qin, Jo Schlemper, Jose Caballero, Anthony N. Price, Joseph V. Hajnal, and Daniel Rueckert. Convolutional recurrent neural networks for dynamic MR image reconstruction. *IEEE Transactions on Medical Imaging*, 38(1):280–290, 2019. Publisher: ieeexplore.ieee.org.
74. M. Jogin, Mohana, M. S. Madhulika, G. D. Divya, R. K. Meghana, and S. Apoorva. Feature extraction using convolution neural networks (CNN) and deep learning. In *2018 3rd IEEE International Conference on Recent Trends in Electronics, Information Communication Technology (RTEICT)*, pages 2319–2323, 2018.
75. Di Zhao, Feng Zhao, and Yongjin Gan. Reference-driven compressed sensing MR image reconstruction using deep convolutional neural networks without pre-training. *Sensors (Switzerland)*, 20(1), 2020.
76. Dong Liang, Jing Cheng, Ziwen Ke, and Leslie Ying. Deep MRI Reconstruction: Unrolled Optimization Algorithms Meet Neural Networks. *arXiv preprint arXiv:1907.11711*, 2019. Publisher: arxiv.org.
77. Dong Liang, Jing Cheng, Ziwen Ke, and Leslie Ying. Deep Magnetic Resonance Image Reconstruction: Inverse Problems Meet Neural Networks. *IEEE Signal Processing Magazine*, 37(1):141–151, 2020. Publisher: ieeexplore.ieee.org.
78. Hai-Miao Zhang and Bin Dong. A Review on Deep Learning in Medical Image Reconstruction. *Journal of the Operations Research Society of China*, 8(2):311–340, June 2020.
79. Dongwook Lee, Jaejun Yoo, Sungho Tak, and Jong Chul Ye. Deep residual learning for accelerated MRI using magnitude and phase networks. *IEEE Transactions on Biomedical Engineering*, 65(9):1985–1995, 2018.
80. Olaf Ronneberger, Philipp Fischer, and Thomas Brox. U-Net: Convolutional networks for biomedical image segmentation. In *Lecture Notes in Computer Science (including subseries Lecture Notes in Artificial Intelligence and Lecture Notes in Bioinformatics)*, volume 9351, pages 234–241. Springer Verlag, may 2015.
81. Christian Ledig, Lucas Theis, Ferenc Huszar, Jose Caballero, Andrew Cunningham, Alejandro Acosta, Andrew Aitken, Alykhan Tejani, Johannes Totz, Zehan Wang, and Wenzhe Shi. Photo-realistic single image super-resolution using a generative adversarial network. In *Proceedings of the IEEE Conference on Computer Vision and Pattern Recognition (CVPR)*, July 2017.
82. Karen Simonyan and Andrew Zisserman. Very deep convolutional networks for large-scale image recognition, 2015.
83. Olga Russakovsky, Jia Deng, Hao Su, Jonathan Krause, Sanjeev Satheesh, Sean Ma, Zhiheng Huang, Andrej Karpathy, Aditya Khosla, Michael Bernstein, Alexander C. Berg, and Li Fei-Fei. Imagenet large scale visual recognition challenge. *International Journal of Computer Vision*, 115(3):211–252, 2015.
84. Roy Shaul, Itamar David, Ohad Shitrit, and Tammy Riklin Raviv. Subsampled brain mri reconstruction by generative adversarial neural networks. *Medical Image Analysis*, 65:101747, 2020.



85. Martin Heusel, Martin Ramsauer, Thomas Unterthiner, Bernhard Nessler, and Sepp Hochreiter. GANs trained by a two time-scale update rule converge to a local nash equilibrium. *arXiv preprint arXiv:1706.08500*, 2018.
86. Christian Szegedy, Vincent Vanhoucke, Sergey Ioffe, Jon Shlens, and Zbigniew Wojna. Rethinking the inception architecture for computer vision. In *Proceedings of the IEEE conference on computer vision and pattern recognition*, pages 2818–2826, 2016.
87. Zhimin Chen and Yuguang Tong. Face Super-Resolution Through Wasserstein GANs. Technical report, 2017.
88. Maciej Wiatrak, Stefano V Albrecht, and Andrew Nystrom. Stabilizing GANs: A Survey Stabilizing Generative Adversarial Networks: A Survey. Technical report, 2020.
89. Martin Arjovsky, Soumith Chintala, and Léon Bottou. Wasserstein GAN. Technical report, 2017.
90. Mingfeng Jiang, Zihan Yuan, Xu Yang, Jucheng Zhang, Yinglan Gong, Ling Xia, and Tieqiang Li. Accelerating CS-MRI Reconstruction with Fine-Tuning Wasserstein Generative Adversarial Network. *IEEE Access*, 7:152347–152357, 2019. Publisher: ieeexplore.ieee.org.
91. Gyutaek Oh, Byeongsu Sim, Hyung Jin Chung, Leonard Sunwoo, and Jong Chul Ye. Unpaired Deep Learning for Accelerated MRI Using Optimal Transport Driven CycleGAN. *IEEE Transactions on Computational Imaging*, 6:1285–1296, 2020. Publisher: ieeexplore.ieee.org.
92. Ishaan Gulrajani, Faruk Ahmed, Martin Arjovsky, Vincent Dumoulin, and Aaron Courville. Improved Training of Wasserstein GANs Montreal Institute for Learning Algorithms. Technical report, 2017.
93. Takeru Miyato, Toshiki Kataoka, Masanori Koyama, and Yuichi Yoshida. Spectral Normalization for Generative Adversarial Networks. *arXiv:1802.05957 [cs, stat]*, February 2018. arXiv: 1802.05957.
94. H. Zhao, O. Gallo, I. Frosio, and J. Kautz. Loss Functions for Image Restoration With Neural Networks. *IEEE Transactions on Computational Imaging*, 3(1):47–57, March 2017. Conference Name: IEEE Transactions on Computational Imaging.
95. Vegard Antun, Francesco Renna, Clarice Poon, Ben Adcock, and Anders C. Hansen. On instabilities of deep learning in image reconstruction and the potential costs of AI. *Proceedings of the National Academy of Sciences*, 117(48):30088–30095, December 2020. Publisher: National Academy of Sciences Section: Colloquium on the Science of Deep Learning.
96. Jingyu Hao, Chengjia Wang, Heye Zhang, and Guang Yang. Annealing genetic gan for minority oversampling. *arXiv preprint arXiv:2008.01967*, 2020.
97. Jin Zhu, Guang Yang, and Pietro Lio. How can we make gan perform better in single medical image super-resolution? a lesion focused multi-scale approach. In *2019 IEEE 16th International Symposium on Biomedical Imaging (ISBI 2019)*, pages 1669–1673. IEEE, 2019.
98. Jin Zhu, Guang Yang, and Pietro Lio. Lesion focused super-resolution. In *Medical Imaging 2019: Image Processing*, volume 10949, page 109491L. International Society for Optics and Photonics, 2019.
99. Qinghao Ye, Jun Xia, and Guang Yang. Explainable ai for covid-19 ct classifiers: An initial comparison study. *arXiv preprint arXiv:2104.14506*, 2021.
100. Guang Yang, Qinghao Ye, and Jun Xia. Unbox the black-box for the medical explainable ai via multi-modal and multi-centre data fusion: A mini-review, two showcases and beyond. *arXiv preprint arXiv:2102.01998*, 2021.